

OPTIMIZATION STUDIES AND FABRICATION OF
AN Fe-Mm(Dy)-B PERMANENT MAGNET USING
POWDER METALLURGY TECHNIQUES

207

by

CHRISTODOULOS N. CHRISTODOULOU

B. S. IN CHEMICAL ENGINEERING
ARISTOTELIAN POLYTECHNION
POLYTECHNIC SCHOOL OF SALONICA-GREECE
1984

A MASTERS THESIS

submitted in partial fulfillment of the

requirements for the degree

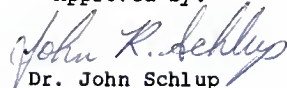
MASTER OF SCIENCE

Department of Chemical Engineering

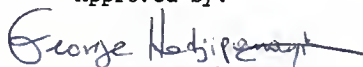
KANSAS STATE UNIVERSITY
Manhattan, Kansas

1987

Approved by:


Dr. John Schlup

Approved by:


Dr. George Hadjipanayis

ACKNOWLEDGMENTS

ALL207 307658

LD
2668
.T4
CHE
1987
C57
c.2

I am grateful to my advisors Dr. John Schlup in Chemical Engineering and Dr. George Hadgipanayis in Physics, for the guidance, encouragement and support that they provided throughout this research.

I would like to thank my thesis committee members, Dr. John Matthews and Dr. Larry Erickson, for the time and effort they gave in evaluating this work.

I would like to thank Dr. Peter Sherwood and his student, Guy Wilson, for assisting in the XPS studies.

I would like to thank Dr. Martin Stoecli for assisting in the deconvolution of the DSC data.

I would also like to thank the members of my research group; particularly, Dr. Brock Dale, Dr. Samy Aly, Dr. Yi Fei Tao, Anton Nazareth, George Nicolaides, Gong Wei; and, especially Lawrence Seib for assisting in the electron microscopy studies.

I wish to thank my loving wife, Filio, for her patience and support throughout this work.

I want to thank Ford Motor Company Electrical and Electronics Division who provided the majority of the funding for this research through the Physics department. A portion of my support was provided by the Chemical Engineering department.

TABLE OF CONTENTS

	Page
ACKNOWLEDGMENTS	i
TABLE OF CONTENTS	ii
LIST OF FIGURES	iv
LIST OF TABLES	xi
CHAPTER 1. INTRODUCTION	1
CHAPTER 2. THEORETICAL BACKGROUND	9
2.1 HYSTERESIS LOOP	9
2.2 MAGNETIZATION PROCESS	11
2.3 MAGNETIC ANISOTROPY	13
2.4 ANISOTROPY FIELD-ANISOTROPY CONSTANT.	14
2.5 CURIE TEMPERATURE	15
2.6 PERMANENT MAGNETS	16
CHAPTER 3. EXPERIMENTAL TECHNIQUES	25
3.1 PROCESSING	25
3.1.1 Alloy Preparation	25
3.1.2 Powder Preparation	25
3.1.3 Aligning and Pressing of Powder in a Magnetic Field	27
3.1.4 Sintering	28
3.2 ANALYSIS	30
3.2.1 Differential Thermal Analysis (DTA)	30
3.2.2 Differential Scanning Calorimetry	30
3.2.3 Particle Size Measurements	31
3.2.4 Magnetic Measurements	31
3.2.5 Density Measurements	32
3.2.6 Microstructure and Magnetic Domain Structure Analysis	33
CHAPTER 4. OPTIMIZATION OF PROCESS PARAMETERS	43
4.1 INTRODUCTION	43
4.2 OPTIMIZATION STUDIES	45
4.2.1 Optimum Particle Size	45
4.2.2 Optimum Aligning Magnetic Field and Compaction Pressure	46
4.2.3 Optimum Temperature and Time of Sintering	47
4.3 DENSITY AS A FUNCTION OF SINTERING TEMPERATURE AND TIME	48
4.4 RESULTS	49
4.4.1 Optimum Particle Size	49
4.4.2 Optimum Aligning Magnetic Field and Compaction Pressure	51
4.4.3 Optimum Temperature and Time of Sintering	52
4.4.4 Density as a Function of Sintering Temperature and Time	52
4.5 DISCUSSION	54
4.6 CONCLUSIONS	57

	Page
CHAPTER 5. OXIDATION OF Fe-R-B POWDERS	
DURING PROCESSING	94
5.1 INTRODUCTION	94
5.2 RESULTS-DISCUSSION	95
5.2.1 Magnetic Properties	95
5.2.2 Differential Scanning Calorimetry	95
5.2.2 X-ray Photoelectron Spectroscopy	97
5.2.3 Estimates of Oxygen Concentration	98
5.2.4 Correlation of DSC Data with Hard Magnetic Properties	99
5.2.5 Application to Processing	100
5.3 CONCLUSIONS	102
CHAPTER 6. HARD MAGNETIC PROPERTIES-THE ORIGIN OF HYSTERESIS	114
6.1 INTRODUCTION	114
6.2 RESULTS OF THERMOMAGNETIC MEASUREMENTS	115
6.2.1 Curie Temperature	115
6.2.2 Coercivity and Remanence as a Function of Temperature	115
6.3 RESULTS FROM MICROSTRUCTURE ANALYSIS.	116
6.3.1 Optical Microscopy	116
6.3.2 Electron Microscopy	116
6.4 RESULTS OF MEASURING MAGNETIC PROPERTIES AS A FUNCTION OF APPLIED FIELD	119
6.4.1 Field Dependence of Coercivity and Remanence	120
6.4.2 Initial Magnetization Curves	120
6.4.3 Magnetic Domains	121
6.5 DISCUSSION-CONCLUSIONS	122
REFERENCES	142
APPENDIX A	149
ABSTRACT TITLE	
ABSTRACT	

LIST OF FIGURES

	Page
Fig. 1.1 Schematic illustration of process for extracting rare-earth elements from ores (Okada, Sugimoto, Ishizaka, Tanaka and Homma [20]). . . .	8
Fig. 2.1.1 Ferromagnetic magnetization curve and hysteresis loop. Important magnetic quantities are illustrated.	17
Fig. 2.2.1 Schematic illustration of domain structure at various stages during the magnetization process. Part I : Reversible wall displacements. Part II : Irreversible wall displacements. Part III : Magnetization rotation. (Chen [25] and Nesbitt [26]).	18
Fig. 2.3.1 Magnetization curve for iron single crystal (Honda and Kaya [55]).	19
Fig. 2.3.2 Magnetization curve for nickel single crystal (Kaya [56]).	19
Fig. 2.3.3 Magnetization curve for cobalt single crystal (Kaya [57]).	20
Fig. 2.4.1 Schematic illustration of magnetization curves obtained when the applied field is parallel and perpendicular to the easy axis of magnetization.	21
Fig. 2.4.2 Magnetization curve of $Nd_2Fe_{14}B$ at 300 K parallel and perpendicular to the easy axis of magnetization [001] (Koon, Das, Rubinstein and Tyson [58]).	22
Fig. 2.5.1 Magnetization versus temperature for $Nd_2Fe_{14}B$ alloy. The Curie temperature is $310^\circ C$ (Güdimetta, Christodoulou and Hadjipanayis [43]).	23
Fig. 3.1.1 Arc-melter used for alloy preparation.	34
Fig. 3.1.2 Batch attritor used for fine powder preparation.	35
Fig. 3.1.3 Carver hydraulic laboratory press in an electromagnet. This system was used for aligning the powder in a magnetic field during pressing. . . .	36
Fig. 3.1.4 System used for sintering the aligned pressed powder.	37
Fig. 3.1.5 Quartz tube used for sample sintering.	38

Fig. 3.2.1 Scanning electron micrograph of powder with 45 min milling time ($D_{avg}=1.2$ microns, magnification=2000).	39
Fig. 3.2.2 Scanning electron micrograph of powder with 150 min milling time ($D_{avg}=0.73$ microns, magnification=4900).	40
Fig. 3.2.3 Various statistical diameters used for particle size measurements. Peret's diameter was used in the present study (Irani and Gallis [30]).	41
Fig. 3.2.4 Vibrating sample magnetometer used for magnetic measurements.	42
Fig. 4.1.1 Schematic illustration of the processes employed for optimization of the final sintered magnets.	59
Fig. 4.2.1 Schematic illustration of the processes employed for optimization of the powder particle size.	60
Fig. 4.2.2 Schematic illustration of the processes employed for optimization of the aligning magnetic field strength, H, and compaction pressure, P.	61
Fig. 4.2.3 Differential thermal analysis (DTA) of $Fe_{74}Mn_{13.5}Dy_{4.8}B_{7.7}$ as-cast alloy showing a phase transformation at $1040^{\circ}C$ (1313 K).	62
Fig. 4.2.4 Schematic illustration of the processes employed for optimization of the sintering temperature and time.	63
Fig. 4.4.1 Arithmetic average particle size (microns) as a function of milling time (minutes).	64
Fig. 4.4.2 Particle size distribution (Percent particles) for a powder milled for zero min. Average diameter=7.01 microns.	65
Fig. 4.4.3 Particle size distribution (Percent particles) for a powder milled for 5 min. Average diameter=5.88 microns.	66
Fig. 4.4.4 Particle size distribution (Percent particles) for a powder milled for 15 min. Average diameter=4.73 microns.	67
Fig. 4.4.5 Particle size distribution (Percent particles) for a powder milled for 25 min. Average diameter=2.63 microns.	68

Fig. 4.4.6 Particle size distribution (Percent particles) for a powder milled for 35 min. Average diameter=1.72 microns.	69
Fig. 4.4.7 Particle size distribution (Percent particles) for a powder milled for 40 min. Average diameter=1.29 microns.	70
Fig. 4.4.8 Particle size distribution (Percent particles) for a powder milled for 45 min. Average diameter=1.20 microns.	71
Fig. 4.4.9 Particle size distribution (Percent particles) for a powder milled for 60 min. Average diameter=1.02 microns.	72
Fig. 4.4.10 Particle size distribution (Percent particles) for a powder milled for 105 min. Average diameter=0.74 microns.	73
Fig. 4.4.11 Particle size distribution (Percent particles) for a powder milled for 150 min. Average diameter=0.73 microns.	74
Fig. 4.4.12 Particle size distribution (Percent particles) for a powder milled for 5, 35, 150 min.	75
Fig. 4.4.13 Coercivity (kOe) of the aligned pressed powders and of the resulting sintered magnets as a function of milling time. The corresponding average particle size (microns) is also shown.	76
Fig. 4.4.14 Remanence (emu/g) of the aligned pressed powders and resulting sintered magnets as a function of milling time. The corresponding average particle size (in units of 0.1 micron) is also shown. . .	77
Fig. 4.4.15 Percent alignment (defined as $(M_r/M_s) \times 100$) of the aligned pressed powder ($D_{avg} = 1.72$ microns) and of the resulting sintered magnets as a function of the aligning magnetic field strength. The compaction pressure is 1.1 kbar. The sintering temperature and time are 1313 K and 15 min, respectively.	78

Fig. 4.4.16 Percent alignment (defined as $(M_r/M_s) \times 100$) of the aligned pressed powder ($D_{avg} = 1.72$ microns) and of the resulting sintered magnets as a function of the aligning magnetic field strength. The compaction pressure is 2.2 kbar. The sintering temperature and time are 1313 K and 15 min, respectively. 79

Fig. 4.4.17 Percent alignment (defined as $(M_r/M_s) \times 100$) of the aligned pressed powder ($D_{avg} = 1.72$ microns) and of the resulting sintered magnets as a function of the aligning magnetic field strength. The compaction pressure is 3.3 kbar. The sintering temperature and time are 1313 K and 15 min, respectively. 80

Fig. 4.4.18 Percent alignment (defined as $(M_r/M_s) \times 100$) of the aligned pressed powder ($D_{avg} = 1.72$ microns) and of the resulting sintered magnets as a function of the aligning magnetic field strength. The compaction pressure is 5.5 kbar. The sintering temperature and time are 1313 K and 15 min, respectively. 81

Fig. 4.4.19 Percent alignment (defined as $(M_r/M_s) \times 100$) of the resulting sintered magnets after pressing the powder ($D_{avg} = 1.72$ microns) at 3.3 kbar or 5.5 kbar as a function of the aligning magnetic field strength. The sintering temperature and time are 1313 K and 15 min, respectively. 82

Fig. 4.4.20 Coercivity of magnets sintered at 1293 K as a function of sintering time (minutes). 83

Fig. 4.4.21 Coercivity of magnets sintered at 1313 K as a function of sintering time (minutes). 84

Fig. 4.4.22 Coercivity of magnets sintered at 1333 K as a function of sintering time (minutes). 85

Fig. 4.4.23 Coercivity of magnets sintered at 1343 K as a function of sintering time (minutes). 86

Fig. 4.4.24 Hysteresis loops of magnets sintered at 1313 K for 15, 30, 60 and 120 minutes. The average particle size of the powder used is 1.72 microns. The compaction pressure is 3.3 kbar. 87

Fig. 4.4.25 Hysteresis loops of magnets sintered at 1343 K for 15, 30, 60 and 120 minutes. The average particle size of the powder used is 1.72 microns. The compaction pressure is 3.3 kbar. 88

Fig. 4.4.26 Coercivity of magnets sintered for 60 minutes as a function of sintering temperature.	89
Fig. 4.4.27 Bulk densities (average of three measurements) and true densities as a function of sintering temperature and time. The density of the as-cast alloy is also shown.	90
Fig. 5.2.1 Differential scanning calorimetry (DSC) data for a solid piece of as-cast alloy with composition $\text{Fe}_{74}\text{Mm}_{13.5}\text{Dy}_{4.8}\text{B}_{7.7}$	103
Fig. 5.2.2 DSC data for $\text{Fe}_{74}\text{Mm}_{13.5}\text{Dy}_{4.8}\text{B}_{7.7}$ powder with average particle size 7.01 microns.	104
Fig. 5.2.3 Deconvoluted DSC curve of $\text{Fe}_{74}\text{Mm}_{13.5}\text{Dy}_{4.8}\text{B}_{7.7}$ powder with an average particle size of 7.01 microns.	105
Fig. 5.2.4 Deconvoluted DSC curve of $\text{Fe}_{74}\text{Mm}_{13.5}\text{Dy}_{4.8}\text{B}_{7.7}$ powder with an average particle size of 5.33 microns.	106
Fig. 5.2.5 Deconvoluted DSC curve of $\text{Fe}_{74}\text{Mm}_{13.5}\text{Dy}_{4.8}\text{B}_{7.7}$ powder with an average particle size of 1.72 microns.	107
Fig. 5.2.6 Deconvoluted DSC curve of $\text{Fe}_{74}\text{Mm}_{13.5}\text{Dy}_{4.8}\text{B}_{7.7}$ powder with an average particle size of 0.91 microns.	108
Fig. 5.2.7 Heats corresponding to each of three peaks and total heat as a function of milling time (particle size in units of 0.1 microns).	109
Fig. 5.2.8 Oxygen concentration (wt%) as a function of milling time (particle size in units of 10 microns).	110
Fig. 5.2.9 Demagnetization curves of sintered magnets prepared using powders with different oxygen concentrations.	111
Fig. 6.2.1 Magnetization versus temperature of an $\text{Fe}_{74}\text{Mm}_{13.5}\text{Dy}_{4.8}\text{B}_{7.7}$ as-cast alloy. The first Curie temperature T_{c1} is 265°C and the second T_{c2} is 290°C.	124
Fig. 6.2.2 Hysteresis loops of $\text{Fe}_{74}\text{Mm}_{13.5}\text{Dy}_{4.8}\text{B}_{7.7}$ sintered magnet as a function of temperature.	125
Fig. 6.2.3 Coercivity (kOe) of $\text{Fe}_{74}\text{Mm}_{13.5}\text{Dy}_{4.8}\text{B}_{7.7}$ sintered magnet as a function of temperature.	126

Fig. 6.2.4 Remanence (emu/g) of $\text{Fe}_{74}\text{Mm}_{13.5}\text{Dy}_{4.8}\text{B}_{7.7}$ sintered magnet as a function of temperature.	127
Fig. 6.3.1 Microstructure of an $\text{Fe}_{74}\text{Mm}_{13.5}\text{Dy}_{4.8}\text{B}_{7.7}$ sintered magnet obtained using optical microscope. A= $\text{Fe}_{14}\text{R}_2\text{B}$ phase, B=rare-earth rich phase.	128
Fig. 6.3.2 Microstructure of an $\text{Fe}_{74}\text{Mm}_{13.5}\text{Dy}_{4.8}\text{B}_{7.7}$ sintered magnet obtained using scanning transmission electron microscope (magnification=2000). (a) Before etching. (b) After etching for few seconds using 3% nital. A= $\text{Fe}_{14}\text{R}_2\text{B}$ phase, B=rare-earth rich phase, C= $\text{Fe}_4\text{R}_1\text{B}_4$ phase.	129
Fig. 6.3.3 Spectra taken using energy dispersive X-ray analyzer in the A regions ($\text{Fe}_{14}\text{R}_2\text{B}$ phase) shown in Figure 6.3.2.	130
Fig. 6.3.4 Spectra taken using energy dispersive X-ray analyzer in the B regions (rare-earth rich phase) shown in Figure 6.3.2.	131
Fig. 6.3.5 Spectra taken using energy dispersive X-ray analyzer in the C regions ($\text{Fe}_4\text{R}_1\text{B}_4$) shown in Figure 6.3.2.	132
Fig. 6.3.6 $\text{Fe}_{14}\text{R}_2\text{B}$ grains pinned by inclusions (possibly oxides, magnification=20000).	133
Fig. 6.4.1 Magnetization curve and demagnetization curves of a thermally demagnetized $\text{Fe}_{74}\text{Mm}_{13.5}\text{Dy}_{4.8}\text{B}_{7.7}$ magnet.	134
Fig. 6.4.2 Magnetization curve and minor hysteresis loops of an ac demagnetized $\text{Fe}_{74}\text{Mm}_{13.5}\text{Dy}_{4.8}\text{B}_{7.7}$ magnet.	135
Fig. 6.4.3 Coercivity as a function of the applied magnetic field for a thermally and ac demagnetized $\text{Fe}_{74}\text{Mm}_{13.5}\text{Dy}_{4.8}\text{B}_{7.7}$ magnet. (Refer at Figure 6.4.1 and 6.4.2).	136
Fig. 6.4.4 Remanence as a function of the applied magnetic field for a thermally and ac demagnetized $\text{Fe}_{74}\text{Mm}_{13.5}\text{Dy}_{4.8}\text{B}_{7.7}$ magnet. (Refer at Figure 6.4.1 and 6.4.2).	137
Fig. 6.4.5 Hysteresis loop of the optimum $\text{Fe}_{74}\text{Mm}_{13.5}\text{Dy}_{4.8}\text{B}_{7.7}$ sintered magnet. The magnetization curves in the thermally and ac demagnetized state are shown for comparison.	138

Fig. 6.4.6 Magnetic domains observed in a thermally demagnetized $\text{Fe}_{74}\text{Mn}_{13.5}\text{Dy}_{4.8}\text{B}_{7.7}$ sintered magnet. 139

LIST OF TABLES

	Page
Table 2.5.1 Curie temperature, T_c , of nine elements.	24
Table 4.4.1 Coercivity H_c (kOe) of $Fe_{74}Mm_{13.5}Dy_{4.8}B_{7.7}$ sintered magnets as a function of sintering temperature T (K) and time t (min).	91
Table 4.4.2 Bulk densities (g/cm^3) of $Fe_{74}Mm_{13.5}Dy_{4.8}B_{7.7}$ sintered magnets as a function of sintering temperature T (K) and time t (min).	92
Table 4.4.3 True densities (g/cm^3) of $Fe_{74}Mm_{13.5}Dy_{4.8}B_{7.7}$ sintered magnets as a function of sintering temperature T (K) and time t (min).	93
Table 5.2.1 Heats (Joule/g) corresponding to each of the three peaks in the DSC data and total heat as a function of milling time (min) and average particle size of the powder (microns).	. . 112
Table 5.2.2 Oxygen concentration (wt%) as a function of milling time (min) and average particle size of the powder (microns). 113
Table 6.2.1 Coercivity H_c (kOe) and remanence M_r (emu/g) of $Fe_{74}Mm_{13.5}Dy_{4.8}B_{7.7}$ sintered magnet as a function of temperature.	. . . 141
Table 6.3.1 Energy dispersive X-ray elemental analysis (mole% based on Fe and rare-earths, boron cannot be detected) of A ($Fe_{1-x}R_xB$), B (rare-earth rich) and C ($Fe_4R_1B_4$) regions shown in Figure 6.3.2. 142

CHAPTER 1

INTRODUCTION

Before magnetic materials can be discussed effectively, a few terms require definition. Coercivity, energy product and Curie temperature are the most important parameters used to describe the strength and applicability of permanent magnets. The coercivity, H_C , is a measure of the material's resistance to demagnetization. The maximum energy product, $(BH)_{\max}$, is a measure of the magnetic energy stored in the magnet. It represents the strength of the magnet. The Curie temperature, T_C , is a measure of resistance to demagnetization with increasing temperature. For high temperature applications a high Curie temperature is needed. These quantities will be discussed in Chapter 2.

Ferrites (lodestone) were the first permanent magnets known thousands years ago. They are widely used today because they are the least expensive magnets. Their $(BH)_{\max}$ is in the range of 3-4 MGOe. AlNiCo magnets with high remanence and small coercivity have been developed for applications such as acoustic devices, telecommunication, and measuring and control devices. A common characteristic for both hard ferrites and AlNiCo magnets is their relatively low energy

product. They have limited applicability in areas such as motors which require high energy products.

The first breakthrough in producing permanent magnets with maximum energy product much greater than those obtained by AlNiCo and ferrites was made by Strnat and his co-workers [1] in 1966. They discovered SmCo_5 magnets with an energy product of 16 MGOe. Further research [2] showed that energy products around 20 MGOe could be achieved. Subsequent development [3,4,5,6] led to more complex compositions based on a $\text{Sm}_2\text{Co}_{17}$ phase where some cobalt has been replaced by iron, zirconium and copper. Magnets with these compositions have energy products as high as 30 MGOe but with lower coercivities.

An attempt was made in the 1970's to substitute expensive samarium with mischmetal (a mixture of rare-earths, mostly light rare-earths). Nagel et al. [7] managed to produce a MmCo_5 magnet (Mm = mischmetal) with a coercivity of 9 kOe and an energy product of 14.5 MGOe. Walkiewicz et al. [8] used Cu and Mg as additives to prepare a Mm-Co-Cu-Mg magnet with an coercivity as high as 29 kOe and a relatively low energy product of 9.2 MGOe.

It is obvious that most of the permanent magnets previously described (e. i., AlNiCo, SmCo_5) contain significant amounts of cobalt as well. This metal is considered to be strategic. An attempt was made in the

late 70's to develop a cobalt-free permanent magnetic material. The early studies had been focused on iron-based alloys because iron has a high magnetic moment and is an abundant element. More recent efforts have been devoted to rapidly quenched R-Fe alloys (R = rare-earth). Studies made on amorphous RFe_2 alloys [9] show large coercivities at cryogenic temperatures. Similar behavior has been observed in other rare-earth systems [10,11]. The hard magnetic properties of these amorphous materials have been observed to increase with the degree of crystallinity. Clark [12] obtained a coercivity of 3.4 kOe and an energy product of 9 MGOe in $TbFe_2$ at room temperature. More recently, Koon et al. [13] have obtained high coercivities in crystallized amorphous $(Fe_{0.8}B_{0.2})_{90}La_5Tb_5$ alloys. However, both of these materials contained Tb which is again an expensive metal. Therefore these materials are not economically favorable. Continuing this effort, Croat et al. [14] produced high coercivities in melt-spun $R_{40}Fe_{60}$ alloys.

A big breakthrough was made in summer, 1982, at Kollmorgen Corporation where Hadjipanayis and co-workers were able to obtain energy products exceeding 12 MGOe in rapidly quenched Fe-R-B-Si alloys. Their results were first presented in April, 1983, and then published in October, 1983 [15]. In the summer of 1983, Sumitomo Special Metals, Japan, announced the first sintered

commercial magnet based on Fe-Nd-B alloys with energy products close to 35 MGOe [16]. In December of 1983, Colt Crucible succeeded to increasing the energy product to 48 MGOe. The unique hard magnetic properties of these materials has been attributed to a new tetragonal phase identified as $Fe_{14}R_2B$ [17,18]. The same tetragonal $Fe_{14}R_2B$ phase is formed with the various rare-earth elements such as Ce, Pr, Nd, Sm, Gd, Tb, Dy, Ho, Er, Tm, and Y [16,17,19].

Recent research interests have been focused on developing low cost Fe-R-B magnets while maintaining high values of the coercivity and energy product. The best candidates to use in substituting for the rare-earth elements are mischmetal and didymium. Both, mischmetal and didymium are mixtures of rare-earth elements and can be obtained during the extraction process of rare-earth elements from ores as is shown in Figure 1.1. Mischmetal is the least expensive of the two. It can be obtained at the very early stages of the chemical treatment. It contains approximately 50%Ce, 25%La, 15%Nd, 5%Pr and 5% other components (3% heavy rare-earths and 2% of Fe, Al, Ca, and Mg). Didymium is less expensive in comparison with pure Nd and can be obtained during the extraction of the light rare-earths (Ce and La) and heavy rare-earths (Sm, Eu and Ga) from mischmetal. The most common compositions of didymium are 90%Nd-10%Pr ,

5%Ce-80%Nd-15%Pr , and 40%Ce-50%Nd-10%Pr.

The most recent and important study was made by Okada et al. [20]. They managed to produce a 5%Ce-didymium-based magnet with a coercivity of $H_c=10.2$ kOe and a maximum energy product of $(BH)_{max}=40$ MGOe. Zhang Maocai et al. [21] developed a magnet with $H_c=6.0$ kOe and $(BH)_{max}=20$ MGOe using the composition $Fe_{73}Nd_{8.5}Mm_{8.5}B_8$.

Recently, Yamasaki et al. [22] used melt spinning techniques to produce ribbons with the composition $Fe_{75}Mm_{16}B_9$ and with $H_c=9.4$ kOe and $(BH)_{max}=8.1$ MGOe. Bonded magnets made of the ribbons have been shown to exhibit a coercivity of 7.6 kOe and an energy product of 4.4 MGOe. These values compare favorably to anisotropic ferrite magnets but are still very small in comparison with the Nd-based magnets.

In the research described herein, a permanent magnet with a composition of $Fe_{74}Mm_{13.5}Dy_{4.8}B_{7.7}$ has been developed [23,24]. The chosen composition is close to the composition used by other researchers who worked on similar Fe-R-B systems [15,16,20,21]. The rare-earth metals contained in Mm as well as Dy produce the $Fe_{14}R_2B$ phase which, as mentioned before, is responsible for the hard magnetic properties. Also, the addition of dysprosium (Dy) contributes to the development of high coercivities which is consistent with the observations

made by other researchers [43,44].

The goals of this research were to develop a mischmetal-based permanent magnet as an alternative with respect to the neodymium-based magnets and to understand and optimize the various process parameters involved during the fabrication of the magnets.

The techniques used to develop the magnet are typical of powder metallurgy. They involve preparation of fine powders, aligning and pressing the powders in a magnetic field, and then sintering at elevated temperatures to achieve a dense product. The optimization studies have been made in order to maximize the magnetic properties of the final sintered magnets. The process parameters that were studied are below.

- 1) Powder particle size.
- 2) Aligning magnetic field strength.
- 3) Compaction pressure.
- 4) Sintering temperature..
- 5) Sintering time.

The impact of the process parameters on the hard magnetic properties and the microstructure of the final optimum sintered magnets will be discussed in Chapters 4 and 6.

During processing, the oxygen adsorbed by the powders appeared to limit the development of the hard magnetic properties of the resulting magnets. When compacts of very fine powders were to be sintered, one could see them burning in the sintering tube, even the sintering atmosphere was oxygen-free. Problems due to the oxidation of the Fe-R-B powders during the preparation of the permanent magnets [23] will be discussed in Chapter 5.

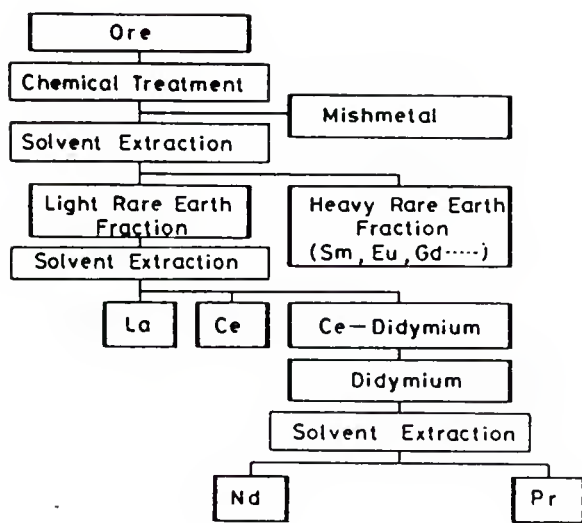


Fig. 1.1 Schematic illustration of process for extracting rare-earth elements from ores (Okada, Sugimoto, Ishizaka, Tanaka and Homma [20]).

CHAPTER 2

THEORETICAL BACKGROUND

2.1 HYSTERESIS LOOP [25,26]

Magnetic hysteresis is an important characteristic of ferro- and ferrimagnetic materials. Figure 2.1.1 shows a typical magnetization curve and hysteresis loop. These curves define the various characteristic magnetic properties of a material. On the application of a magnetic field H , a net magnetization, M , is established. Upon plotting the value of magnetic induction, $B=H+4\pi M$, as a function of H , curve 1 is obtained. The value of B , when saturation magnetization, M_s , is reached for that particular applied field, is referred to as B_s . If the applied field is reduced to zero, the value of B does not return to zero but traces curve 2 to the point B_r which is called residual induction. If the H field is now reversed in direction and increased in the negative direction, the curve continues along 2 until B equals $-B_s$. If H is again decreased to zero and then reversed in direction, curve 3 will be obtained and the hysteresis loop will be completed. H_c is the coercive force. It is the reverse field required to reduce the magnetic induction, B , to zero. When the magnetization, M , is plotted versus H , the saturation magnetization, M_s , residual

magnetization, M_r , and intrinsic coercivity, mH_c , are used instead of B_s , B_r and bH_c , respectively. Therefore, mH_c is the field necessary to reduce the magnetization, M , to zero.

For rare-earth-based permanent magnets, mH_c is usually larger than bH_c . For the AlNiCo type magnets, in which B is usually much larger than H , the values of mH_c and bH_c are approximately equal. The value of $(BH)_{\max}$ indicated in the second quadrant of Figure 2.1.1 is known as the maximum energy product. This point represents the optimum condition in which a given amount of magnetic flux will be carried by the smallest amount of material. For a square shape hysteresis loop ($bH_c=B_r$) the maximum energy product is given by:

$$(BH)_{\max} = (B_r/2)^2 \quad [27]$$

2.2 MAGNETIZATION PROCESS [25,26]

A ferromagnetic material in the demagnetized state is divided into a number of small regions called domains. Each domain is spontaneously magnetized to the saturation value M_s , but various domains have different directions of magnetization so in the absence of the magnetic field there is no net magnetization. The boundary layers between domains are known as domain walls.

The process of magnetizing a ferro- or ferrimagnetic material involves the movement of domain walls [25,46,47,48,49] and subsequent rotation of the magnetization vectors of the domains. Figure 2.2.1 illustrates schematically how the domain structure of a magnetic material with cubic structure changes as it is magnetized to saturation. Initially in this schematic there are four triangular domains (sample demagnetized, zero net magnetic moment), which finally at high fields become a single domain oriented in the direction of the applied field. Domain wall motion is the mechanism for magnetization process in low applied fields, whereas rotation of the atomic moments is the mechanism for high applied fields.

Generally, an initial magnetization curve (Fig. 2.2.1) is divided into three parts. The first part extends from the toe (O) to the instep (A)

(small fields) and is reversible. The second part covers the steepest segment of the curve between the instep and the knee (B). The slope rises very rapidly to a maximum value. It then drops off gradually. The third part lies above the knee (B) and ultimately reaches the saturation value of magnetization, M_s . Both the second and third parts of the magnetization curve are irreversible [25].

2.3 MAGNETIC ANISOTROPY

The magnetization curve can have different shapes depending on whether the specimen is a single crystal or polycrystalline, the predominant orientation of the crystals, the state of stress of the material, the temperature and other factors [26,46,47,48,49].

Shown in Figures 2.3.1, 2.3.2 and 2.3.3 are the magnetization curves for single crystal specimens of Fe and Ni with the magnetizing field applied in the [100], [110] and [111] directions and curves for Co single crystals with the field applied in the [0001] and [uvw0] directions. For each metal there are crystal directions in which the magnetization is attained at all levels with ease. Such directions are called the easy axes, or directions of easy magnetization. For Fe, Ni, and Co, the easy directions are $\langle 100 \rangle$, $\langle 111 \rangle$, and [0001], respectively. There are also directions of hard magnetization in which the process of magnetization encounters the greatest difficulty. The hard directions for Fe, Ni and Co are $\langle 111 \rangle$, $\langle 100 \rangle$, and [uvw0], respectively. This phenomenon of showing crystallographic preference for magnetization is known as the magnetocrystalline anisotropy.

2.4 ANISOTROPY FIELD - THE ANISOTROPY CONSTANT

High magnetic anisotropies are important in determining the properties of permanent magnet materials [15,16]. Highly anisotropic materials like rare-earth based magnets, exhibit high coercivities [33,34]. The anisotropy constant can be estimated by determining the magnetization behavior in the easy and hard directions (Fig. 2.4.1) of single crystals or of magnetically aligned powders in wax [26,46]. The anisotropy field, H_a , is estimated by extrapolating the hard axis curve to saturation. Thus, the anisotropy field, H_a , is the field required to rotate the magnetization into the hard direction or the field required to saturate the material in the hard direction. Then the anisotropy constant, K , for the simplest case (uniaxial materials) is given by the equation below.

$$K = H_a * M_s / 2 \quad [46]$$

The magnetization of $Fe_{14}Nd_2B$ at 300 K for the easy and hard axis is shown in Figure 2.4.2. The anisotropy field and anisotropy constant for the same material are 76 kOe and 4.9×10^7 erg/cm³, respectively.

2.5 CURIE TEMPERATURE [25,28]

All ferromagnetic materials exhibit a characteristic temperature known as the Curie temperature, T_c . This is the critical temperature at which thermal energy is just sufficient to destroy the spontaneous magnetization. Thus, the Curie temperature marks the transition point at which a ferromagnet becomes paramagnetic upon heating. The Curie temperature of nine elements are listed in Table 2.5.1. A typical plot of magnetization of $Fe_{14}R_2B$ as a function of temperature is shown in Fig. 2.5.1.

2.6 PERMANENT MAGNETS

A permanent magnet is designed to provide a source of magnetism which does not require an external energy source to maintain a magnetic field. It must also be able to retain its magnetism for an unlimited time period even under the action of limited demagnetizing influences. The actual magnetic strength, or flux, in a permanent magnet is dependent upon the material from which is made and its processing history [26,33,46].

The essential characteristics of a permanent magnet material after it has been magnetized are coercivity (H_C), residual magnetization or remanence (M_r) and energy product value ($(BH)_{\max}$) [33].

The coercivity, H_C , (Fig. 2.1.1) is a measure of the material's resistance to demagnetization.

The remanence, M_r , relates to the intensity of magnetism remaining in the magnet at zero magnetizing field. The energy product value, $(BH)_{\max}$, is the quantity of magnetic energy stored in the magnet following magnetization.

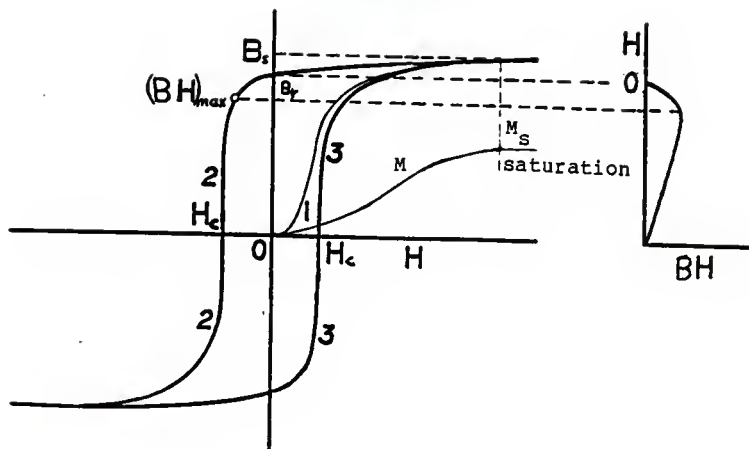


Fig. 2.1.1 Ferromagnetic magnetization curve and hysteresis loop. Important magnetic quantities are illustrated.

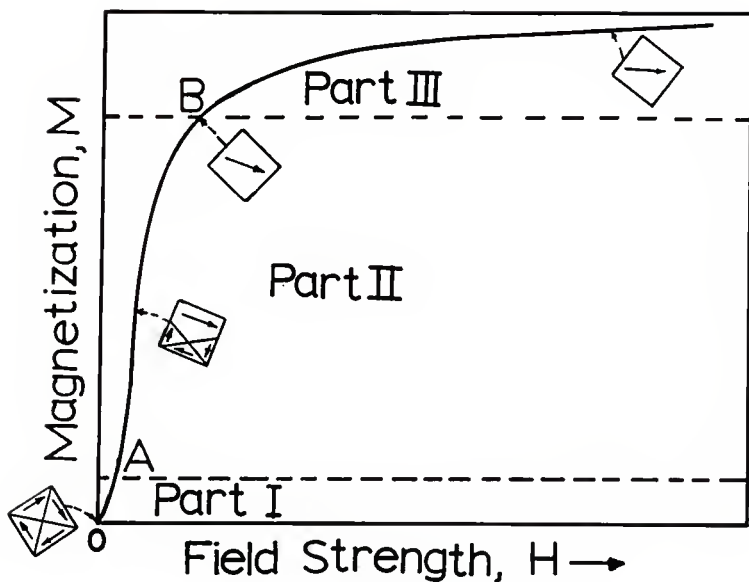


Fig. 2.2.1 Schematic illustration of domain structure at various stages during the magnetization process.
 Part I : Reversible wall displacements.
 Part II : Irreversible wall displacements.
 Part III : Magnetization rotation.
 (Chen [25] and Nesbitt [26]).

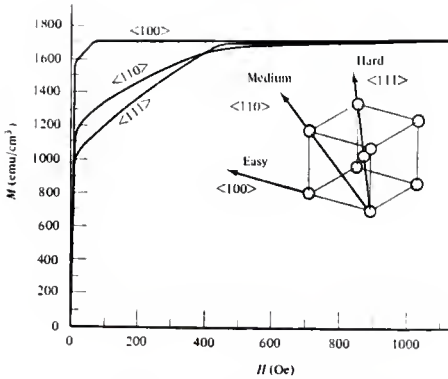


Fig. 2.3.1 Magnetization curves for iron single crystal (Honda and Kaya [55]).

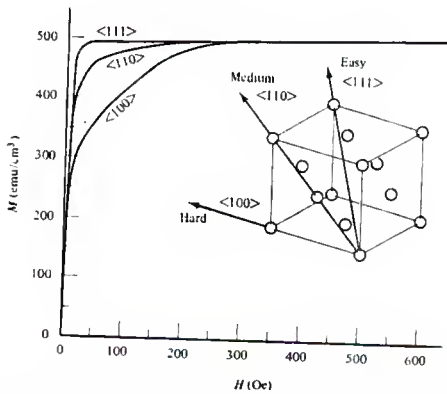


Fig. 2.3.2 Magnetization curves for nickel single crystal (Kaya [56]).

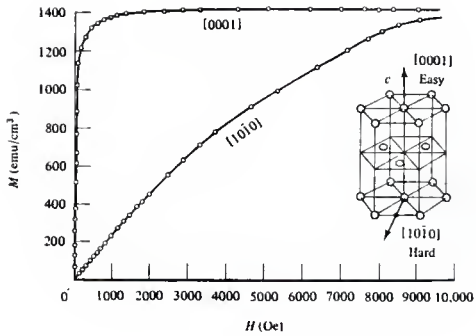


Fig. 2.3.3 Magnetization curves for cobalt single crystal (by Kaya [57]).

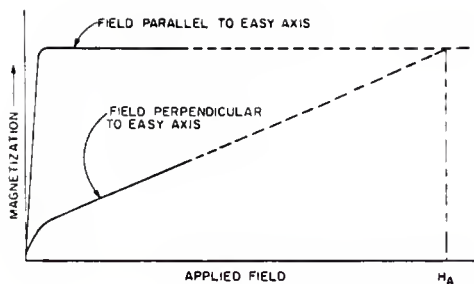


Fig. 2.4.1 Schematic illustration of magnetization curves obtained when the applied field is parallel and perpendicular to the easy axis of magnetization.

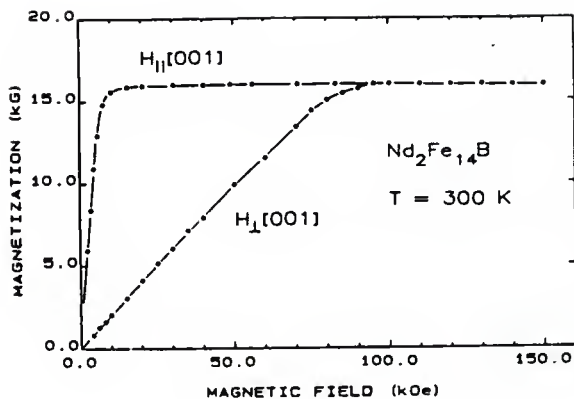


Fig. 2.4.2 Magnetization curves of $Nd_2Fe_{14}B$ at 300 K parallel and perpendicular to the easy axis of magnetization [001] (Koon, Das, Rubinstein and Tyson [58]).

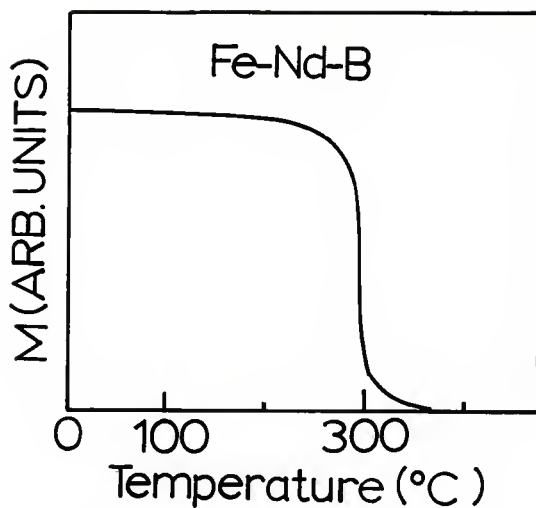


Fig. 2.5.1 Magnetization versus temperature for the $\text{Nd}_2\text{Fe}_{14}\text{B}$ alloy. The Curie temperature is 310°C (Gudimetta, Christodoulou and Hadjipanayis [43]).

Table 2.5.1

Curie temperature of nine elements (Chen [25]).

METAL	Curie Temperature	
	(K)	(C)
Iron	1043	770
Cobalt	1400	1127
Nickel	631	358
Gadolinium	293	20
Terbium	220	-53
Dysprosium	88	-185
Thulium	32	-241
Erbium	20	-253
Holmium	19	-254

CHAPTER 3

EXPERIMENTAL TECHNIQUES

3.1 PROCESSING

3.1.1 Alloy Preparation

The as-cast alloy with the composition $\text{Fe}_{74}\text{Mm}_{13.5}\text{Dy}_{4.8}\text{B}_{7.7}$ was made into 8.0 g buttons by arc-melting in a high purity argon atmosphere. The purity of the iron and dysprosium used was 99.99 % or better. Ferroboron (FeB) having a composition of 81.7 wt% iron and 18.3 wt% boron was used instead of elemental boron because of the lower melting point of FeB. The composition (in wt%) of the mischmetal (Mm) used was 50% Ce, 25% La, 15% Nd, 5% Pr and 5% other components (3% heavy rare-earth and 2% Fe, Ca, Mg and Al). After melting, the buttons were etched with dilute HNO_3 for a few seconds to remove oxides present on the surface. Figure 3.1.1 is a photograph of the arc-melter used to prepare the as-cast alloy.

3.1.2 Powder Preparation

A. Coarse Powder

The as-cast alloy was crushed into small pieces having diameters of 2-5 mm using a stainless steel

mortar. The pieces were transferred into the chamber of a micro-mill and crushed further under an argon gas atmosphere. During pulverization the powder was cooled using a water jacket around the micro-mill chamber. Approximately 30 g of alloy were used for each micro-mill operation. The average particle size achieved at this stage was approximately 500 microns or less (-35 mesh). The resulting powder (<500 microns) was crushed further using the stainless steel mortar until it passed through a 100 mesh sieve (<150 microns). During crushing in the mortar, the powder was kept wet with methylene chloride and it was protected with an argon atmosphere. Methylene chloride (boiling point 313 K) was used to absorb the heat generated during milling. The argon gas minimized the exposure of powder to atmospheric oxygen. The final powder (<150 microns) was kept under moisture-free toluene to protect it from oxidation.

B. Fine Powder

For optimum magnetic properties, a fine powder is needed. The coarse powder (<150 microns) was ground further by ball-milling. The resulting powder was transferred into the chamber of a batch attritor to which stainless steel balls were added (Fig. 3.1.2). Toluene was added to cover the batch. The toluene

absorbed the heat generated during milling and prevented exposure of the powder in atmospheric oxygen.

Milling proceeds by agitating the batch using an impeller rotating at 70 rpm. Samples were taken at different milling time intervals. Samples taken from the batch were labeled and kept under toluene.

3.1.3 Aligning and Pressing of Powder in a Magnetic Field

Wet powder was transferred into a die. The die was placed in a Carver hydraulic laboratory press and positioned in a magnetic field produced by an electromagnet (Fig. 3.1.3). Rectangular green compacts were prepared having dimensions of 3.175mm x 3.175mm x 6.0mm. Pressures up to 5.5 kbar could be used with the given die. Magnetic fields from 0.5 to 8.0 kOe were used to align the powders.

The following procedure was used for aligning and pressing the powder. First the die was moved to the area between the poles of the electromagnet by raising the base of the press. The desired magnetic field was applied. The powder then was pressed at the desired pressure in a direction perpendicular to the magnetic field. The magnetic field was removed followed by release of the pressure.

3.1.4 Sintering [29]

Sintering is the high temperature heat treatment used to consolidate the pressed powder into an integral body with high density and mechanical strength. The system used for sintering is shown in Fig. 3.1.4. It is consisted of the components listed below.

- 1) System of vacuum and argon gas lines allowing vacuum or inert atmospheres in the region of the sintering tube containing the sample.
- 2) A quartz sintering tube (Fig. 3.1.5) with a thermocouple positioned where the sample is to be placed.
- 3) A high temperature (up to 1400 K) tube furnace with a temperature controller permitting control within ± 1 K.

The aligned pressed powder was placed inside the sintering tube and the tube was evacuated. The vacuum helps to remove the toluene present on the powder. After 10 minutes the sintering tube was flushed with argon. Repeated evacuation with subsequent flushing with argon was used to obtain an oxygen-free atmosphere. The sintering tube was slowly pushed in the tube furnace which previously had been stabilized at the desired temperature. During sintering $15 \text{ cm}^3/\text{sec}$ (2.0 SCF per hour) argon flowed over the sample to

maintain oxygen-free conditions. After sintering, the sintering tube was pulled from the tube furnace to cool to room temperature. The sintered magnets were polished with sand-paper and cut into small pieces suitable for magnetic measurements.

3.2 ANALYSIS

3.2.1 Differential Thermal Analysis (DTA)

Differential Thermal Analysis (DTA) can give very important information regarding phase transitions and other temperature dependent processes. DTA is based on measuring the temperature difference between the sample under investigation and a reference sample as a function of temperature of the sample. The temperature of the reference sample increases or decreases linearly (no phase transition). If the sample undergoes a transformation with an associated latent heat during heating or cooling, then temperature differences can be observed as minima or maxima in the DTA curve.

DTA experiments were made using a DuPont 1090 thermal analyzer.

3.2.2 Differential Scanning Calorimetry (DSC)

Differential Scanning Calorimetry (DSC) is based on measuring the heat generated or absorbed as a function of temperature. DSC data can be very useful in describing endothermic and exothermic reactions or other transformations taking place upon heating or cooling.

Differential Scanning Calorimetry (DSC) measurements were made using a DuPont 910 differential scanning calorimetry.

3.2.3 Particle Size Measurements [30]

The wet sample was first dried under vacuum and then homogenized. A representative sample was taken and placed on the one side of a double-sided masking tape which was glued on a microscope grid. Then the powder was coated with gold using vapor deposition.

The particle size was measured using electron micrographs of the coated samples obtained with Jeol 100C scanning transmission electron microscope. Typical electron micrographs are shown in Fig. 3.2.1 and Fig. 3.2.2 for milling times 45 and 150 min, respectively. More than 500 particles were used to determine each particle size distribution. Since the particles were not spherical in shape but irregular, Feret's horizontal diameter was measured for each particle, as shown in Fig. 3.2.3.

3.2.4 Magnetic Measurements [31]

Hysteresis loops were taken using the vibrating sample magnetometer (VSM) shown in Fig. 3.2.4. Field strengths as large as 17 kOe were used. Thermomagnetic data were taken using the high temperature (up to 1000 K) VSM probe with an applied magnetic field less than 1 kOe.

3.2.5 Density Measurements [32]

Densities were measured using ASTM Procedure C 135-66 for true and bulk density of refractory materials [32]. The procedure below was used.

- 1) Measure the mass of a clean dried pycnometer (m_1).
- 2) Fill the pycnometer with double distilled water, stabilize the temperature at 25°C. The total mass (m_2) is measured.
- 3) Remove the water and dry the pycnometer. Put the sample under investigation in the pycnometer and measure the total mass (m_3).
- 4) Fill the pycnometer with double distilled water, stabilize the temperature at 25°C and measure the mass (m_4).
- 5) Estimate the bulk density (d) of the sample using the formula:

$$d = d_w * (m_3 - m_1) / (m_2 + m_3 - m_1 - m_4)$$

where $d_w = 0.997 \text{ g/cm}^3$ (the density of water at 25°C).

For the 1st and 2nd steps, three successive measurements requiring masses to agree to 0.001 g were required for consistency.

To measure the true density the samples were ground into fine powder using a mortar. The above procedure was used with that powder.

3.2.6 Microstructure and Magnetic Domain Structure Analysis

A Jeol 100C scanning transmission electron microscope with an energy dispersive X-ray analysis unit was used to examine the microstructure and chemical composition of the phases present in the samples. A Leitz optical microscope was employed to observe the grain structure of the samples as well.

A Hitachi HU-11B transmission electron microscope was used to observe the magnetic domains. The contrast between the under-focused and over-focused pictures was employed to identify the magnetic domains [46].

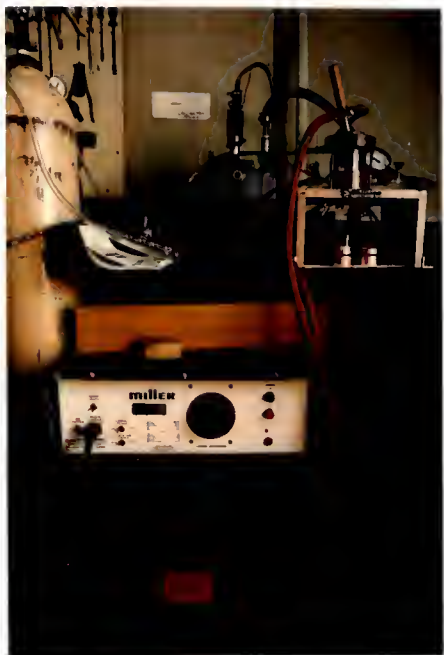


Fig. 3.1.1 Arc-melter used for alloy preparation.



Fig. 3.1.2 Batch attritor used for fine powder preparation.



Fig. 3.1.3 Carver hydraulic laboratory press in an electromagnet. This system was used for aligning the powder in a magnetic field during pressing.

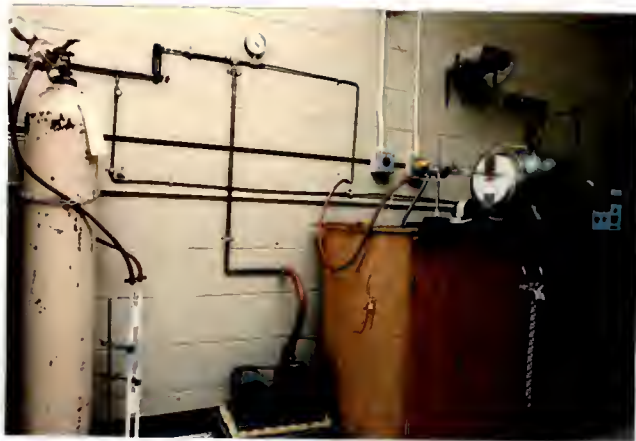


Fig. 3.1.4 System used for sintering the aligned pressed powder.

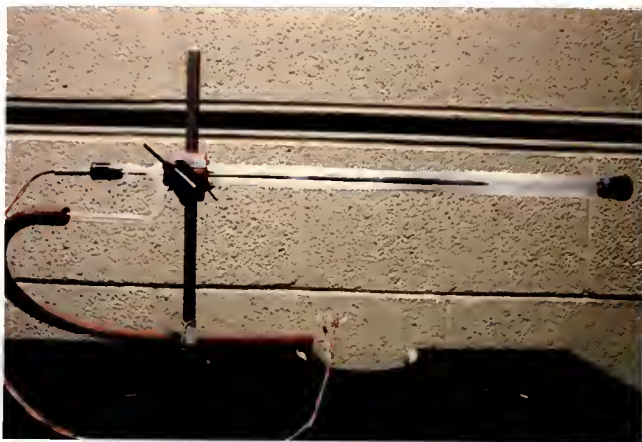


Fig. 3.1.5 Quartz tube used for sample sintering.

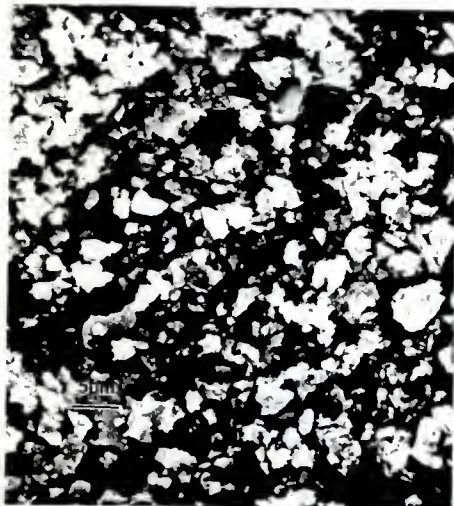


Fig. 3.2.1 Scanning electron micrograph of powder with 45 min milling time ($D_{\text{avg}}=1.2$ microns, magnification=2000).

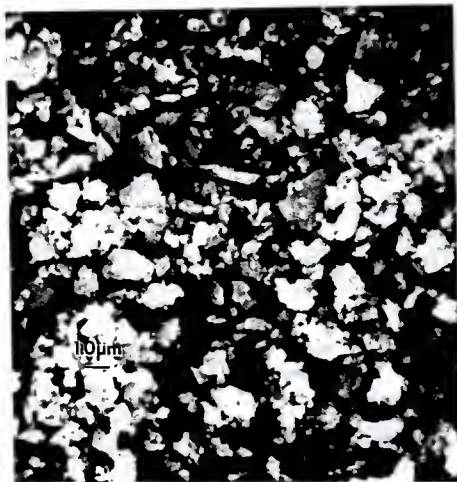


Fig. 3.2.2 Scanning electron micrograph of powder with 150 min milling time ($D_{avg}=0.73$ microns, magnification=4900).

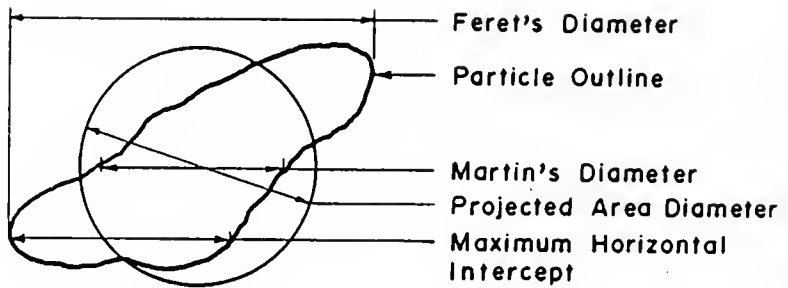


Fig. 3.2.3 Various statistical diameters used for particle size measurements. Feret's diameter was used in the present study (Irani and Gallis [30]).

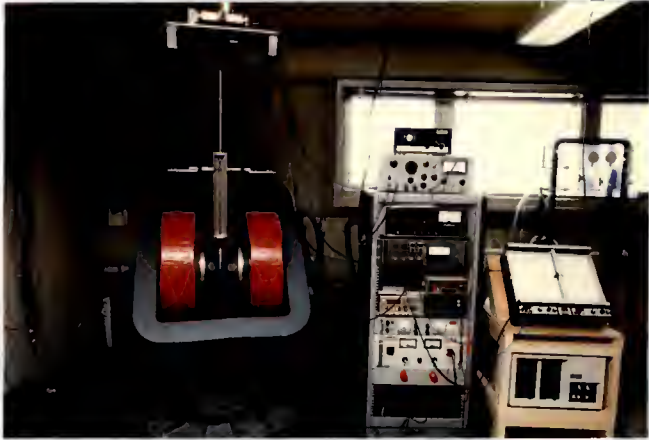


Fig. 3.2.4 Vibrating sample magnetometer used for magnetic measurements.

CHAPTER 4

OPTIMIZATION OF PROCESS PARAMETERS

4.1 INTRODUCTION

The hard magnetic properties of a material are strongly dependent on its processing history. During fabrication of permanent magnets the five process parameters listed below have been shown to significantly impact the final magnetic properties [26,33,46].

1. Powder particle size.
2. Aligning magnetic field
3. Compaction pressure
4. Temperature of sintering
5. Time of sintering

Optimization of these parameter will lead to maximum hard magnetic properties (high coercivity, H_c , and remanence, M_r) [16,20,33,45].

First, 200 g coarse powder (<150 microns) of an alloy with composition $Fe_{74}Mn_{13.5}Dy_{4.8}B_{7.7}$ was prepared as described in Section 3.1.2. It was ball-milled for 5 min under moisture-free toluene using an attrition mill. The resulting powder had an average particle size of 7.01 microns. Subsequent processing was divided into four stages as shown in Fig. 4.1.1.

Half amount of the powder (100 g) was used to optimize the particle size. The magnetic properties of the aligned pressed powders and resulting sintered magnets were measured as a function of the milling time and particle size.

Following optimization of the milling time the rest of the powder (100 g) was attrition milled at the optimum milling time. This powder was used to optimize the strength of the aligning magnetic field, H , and the compaction pressure, P . These conditions of H and P were used in optimizing the temperature and time for sintering.

It is very important to achieve high densities after sintering. High density magnets lead to higher remanent magnetic induction and therefore higher energy product. Also, high densities may reduce the possibility of macroscopic corrosion of the magnets [33].

4.2 OPTIMIZATION STUDIES

4.2.1 Optimum Particle Size

The procedure used to optimize the size of the initial powder (average diameter=7.01 microns) is shown in Fig. 4.2.1. First, powder with an average diameter of 7.01 microns was attrition milled further using time intervals as described in Section 3.1.2. Sixteen different milling times were used with the longest being 150 min. A 3 g sample was taken from the initial batch for each milling time studied.

The particle size distribution of each sample was obtained using a scanning transmission electron microscopy. Differential scanning calorimetry data were obtained for each sample to determine if reactions or phase changes occur in the powder with increasing temperature. The importance of these experiments will be discussed extensively in Chapter 5.

A portion of the sample powder was aligned and pressed uniaxially. The resulting green compacts were sintered as described in Sections 3.1.3 and 3.1.4. An aligning magnetic field of 8.0 kOe and compaction pressure of 3.3 kbar were used. The sintering temperature and time used were 1313 K and 15 min, respectively. These values were strongly suggested from

preliminary experiments and experience based on studies on similar alloys. The magnetic properties of the aligned pressed powders and the resulting sintered magnets were measured using a vibrating sample magnetometer. The powder forming sintered magnets having maximum coercivity and remanence was considered to have the optimum particle size.

4.2.2 Optimum Aligning Magnetic Field Strength and Compaction Pressure

The procedure used to optimize the aligning magnetic field strength and compaction pressure is shown in Fig. 4.2.2. Powder having the optimum particle size determined above was used. Aligning and pressing in a magnetic field were done according to the procedure described in Section 3.1.3. A range of values between 0.5-8.0 kOe and 1.1-5.5 kbar were used for the aligning magnetic field strength and compaction pressure, respectively. Sintering was done at 1313 K for 15 min as described in Section 3.1.4. Magnetic measurements were done using a VSM. The optimum aligning field strength and compaction pressure were considered to be that pair of H and P values for which the fabricated sintered magnet had the maximum percent alignment (defined as $(M_r/M_s) \times 100$) and maximum coercivity.

4.2.3. Optimum Temperature and Time of Sintering

Sintering was done as described in Section 3.1.4. The sintering temperature and time were varied from 1293-1343 K and 15-120 min, respectively. The temperature range was suggested by the phase transformation observed from the DTA data shown in Figure 4.2.3. Figure 4.2.4 illustrates the procedure used for these experiments.

4.3 DENSITY AS A FUNCTION OF SINTERING TEMPERATURE AND TIME

It is very important to maximize the mass density of the sintered magnets because the energy product which measures the strength of the magnet, is proportional to the mass density squared. Density measurements were done based on the ASTM C 135-66 as described in Section 3.2.5.

4.4 RESULTS

4.4.1 Optimum Particle Size

A. Particle Size Distribution as a Function of Milling Time

The arithmetic average particle size as a function of milling time is shown in Fig. 4.4.1. As the milling time increases the decrease in average particle size is approximately exponential. For the first 35 min the reduction in particle size is approximately 75 % and reaches 90 % for 150 min.

Particle size distributions for milling times of zero, 5, 15, 25, 35, 40, 45, 60, 105 and 150 min are shown in Figures 4.4.2 through 4.4.11, respectively. For short milling times the particle size distribution is large and with an asymmetric gaussian shape. For longer milling times the particle size distribution becomes symmetric with the maximum in the distribution shifting to smaller sizes. For example, for zero milling time 81 % of the particles are between 3 and 10.5 microns in diameter. For 35 min milling time, 89 % of the particles have diameters between 1 and 2.5 microns. A comparison of the particle size distribution for the milling times of 5, 35 and 150 min is shown in Fig. 4.4.12.

B. Coercivity and Remanence as a Function of Milling Time

The coercivity of the aligned pressed powders and the resulting sintered magnets as a function of milling time is shown in Fig. 4.4.13. In the aligned pressed powders the coercivity increases monotonically with increasing milling time. The coercivity of the resulting sintered magnets initially increases, passes through a maximum, and then decreases drastically.

The remanence for the aligned pressed powders and the resulting sintered magnets as a function of milling time is shown in Fig. 4.4.14. The remanence for the aligned pressed powder initially increases, passes through a flat maximum and then decreases slowly. In the case of the corresponding sintered magnets, the behavior is similar, except that the remanence of the sintered samples drops drastically after the maximum. This behavior is similar to that of the coercivity. The maximum for both coercivity and remanence correspond to particles with a milling time of 35 min. The average particle size corresponding to a milling time of 35 min is 1.72 microns. Therefore, the optimum particle size yielding maximum coercivity and remanence is 1.72 microns. The reasons for the dramatic decrease in coercivity and remanence of the sintered magnets prepared from powders having an average diameter less

than 1.72 microns are the subject of Chapter 5.

4.4.2 Optimum Aligning Magnetic Field Strength and Compaction Pressure

The procedure followed is described in Section 4.2.2. The percent alignment (defined as $(M_r/M_s) \times 100$) of the aligned pressed powders and resulting sintered magnets as a function of the aligning magnetic field strength and compaction pressure is shown in Figures 4.4.15 through 4.4.18 for compaction pressures of 1.1, 2.2, 3.3, and 5.5 kbar, respectively. Magnetic field strengths of 0.5, 1, 1.5, 2, 4, 6, and 8 kOe were used at each compaction pressure. Three replicates were used for each data point.

It appears that for the compaction pressures studied, there is a threshold aligning field strength of 2 kOe for an alignment of 93 % . The improvement of alignment using fields between 2 and 8 kOe is about 0-3 % in absolute units depending on the compaction pressure. The optimum aligning magnetic field strength is 8 kOe and the optimum compaction pressure is 3.3 kbar. The achieved alignment for these optimum values is 96 % (Fig. 4.4.17). For comparison, Fig. 4.4.19 shows the alignment for the sintered magnets as a function of applied field for compaction

pressures of 3.3 and 5.5 kbar.

4.4.3 Optimum Temperature and Time of Sintering

Table 4.4.1 shows the coercivity as a function of temperatures and times of sintering. Three replicates experiments were used for each temperature-time pair. The coercivity as a function of sintering time is shown in Fig. 4.4.20 through 4.4.23 for temperatures of 1293, 1313, 1333 and 1343 K, respectively. The hysteresis loops at temperatures equal to 1313 K and 1343 K for different sintering times are shown in Fig. 4.4.24 and Fig. 4.4.25, respectively.

At all the sintering temperatures there is an optimum sintering time yielding a maximum coercivity. This optimum sintering time decreases with increasing temperature. The optimum temperature is 1313 K and after sintering for 60 min, the coercivity takes the maximum value of 12.10 kOe. Figure 4.4.26 shows the coercivity obtained for a sintering time of 60 min at 1293, 1313, 1333 and 1343 K.

4.4.4 Density as a Function of Sintering Temperature and Time

For the sintering temperatures and times studied, the bulk and true density of the resulting sintered magnets were measured. The results are

given in Tables 4.4.2 and 4.4.3. These data are plotted in Fig. 4.4.27.

The bulk density of the as-cast alloy (in this case equal to the true density of the as-cast alloy) is found to be 7.459 g/cm^3 . The true density of the sintered magnets is found to be very close to the bulk density of the as-cast alloy. The bulk density of the sintered magnets is found to increase with increasing the sintering temperature and time. In the case of the optimum sintered magnets (sintering temperature 1313 K and time 60 min), the bulk density is 7.31 g/cm^3 , which is the 98% of that of the as-cast alloy.

4.5 DISCUSSION

The results of the optimization studies show clearly the effect and importance of each parameter studied.

The single grain size of the as-cast alloy was observed using scanning transmission electron microscope and was found to be approximately 5 microns. Milling produces a narrow size distribution of single crystal particles; ie., individual particles containing no grain boundaries and therefore only one preferred axis of magnetization. This was suggested from the remanence versus particle size data where for particle sizes less than the single grain size the remanence was constant (Fig. 4.4.14). The importance of average particle size for magnets fabrication is very critical. Overmilling produces excess oxygen pick-up and causes a drastic deterioration of the hard magnetic properties after sintering. This issue is extensively discussed in Chapter 5, where a correlation between oxygen concentration and hard magnetic properties is demonstrated.

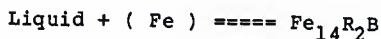
The degree of alignment is influenced by the strength of the aligning magnetic field and compaction pressure. From the results it is clear that for a given pressure the maximum applied aligning magnetic field produces the maximum degree of alignment. This was

expected because the higher fields exert larger forces on the particles during alignment. The most critical range for the aligning magnetic field is between 0.5 and 2 kOe. In this range, for a given pressure, the degree of alignment increases exponentially. Field strength of 2 kOe appears to be the threshold field for an alignment 93 %. A maximum alignment of 96 % was achieved for the maximum aligning field (8 kOe) studied.

The effect of compaction pressure is also very important. There is an optimum compaction pressure (3.3 kbar) which is sufficient to give the powder compact enough mechanical strength to withstand handling but not high enough to cause particle misalignment. This pressure eliminates the mobility of particles in the powder compacts; therefore, misalignment forces acting during sintering, like surface tension, are minimized. This is quite obvious for small compaction pressures. For example, for the compaction pressure of 1.1 kbar and aligning magnetic field strength of 0.5 kOe the alignment for the powder is 80.9 %. After sintering it decreases to 80.1 %. This can be explained by the fact that for small compaction pressures the particles are loose and the compact has significant void volume. During sintering movement of particles during shrinkage causes distortion of the alignment. The negative effect of high compaction pressures and low aligning

magnetic field is also very obvious. For the pressure of 5.5 kbar and magnetic field of 0.5 kOe the degree of alignment is 81.0 %. After sintering it decreases to 79.5 %. This happens because of the distortion of alignment produced by the high pressures.

The effect of sintering temperature and time is very important. It was not surprising to find that the optimum temperature of 1313 K was exactly the temperature suggested by the DTA data (Fig. 4.2.3). This temperature possibly corresponds to the peritectic reaction [29] :



Therefore this temperature provides the liquid phase for more effective sintering by means of growth of the $\text{Fe}_{14}\text{R}_2\text{B}$ phase and densification. The phenomena occurring during sintering and eventually the magnetic properties of the resulting sintered magnet are time dependent. A sintering time of 60 min is found to be optimum. This time of 60 min seems to agree generally with similar studies made on other systems like Fe-Nd-B [16].

Densification proceeds very fast (Fig. 4.4.27). For the optimum conditions of 1313 K and 60 min the achieved density of the sintered magnet takes the value of 7.31 g/cm^3 which corresponds to 98 % of the density of the as-cast alloy. This density is considered to be high [33].

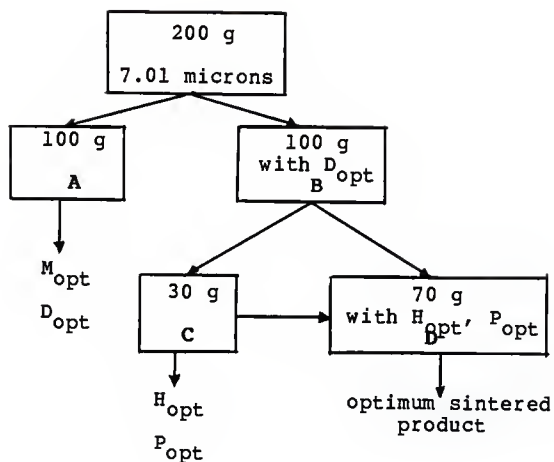
4.6 CONCLUSIONS

The conclusions taken from the processing data are listed below.

1. There is an optimum average particle size of 1.72 microns for which the resulting sintered magnets have maximum hard magnetic properties ($H_c=12$ kOe, $M_r=80$ emu/g).
2. The optimum aligning magnetic field strength is found to be 8 kOe. The optimum uniaxial compaction pressure is 3.3 kbar. The alignment for the resulting sintered magnets is 96 %. There appears to be a threshold magnetic field of 2 kOe required for an alignment of 93 %.
3. The optimum sintering temperature and time are found to be 1313 K and 60 min, respectively. The bulk density achieved under these optimum conditions is 7.31 g/cm^3 which corresponds to 98 % of the bulk density of the as-cast alloy.

These concepts can be generalized for all the similar alloy-systems for which powder metallurgical processing is used for fabrication. The absolute values of the parameters involved will change depending on the particular alloy composition being studied.

For the alloy under investigation
($\text{Fe}_{74}\text{Mn}_{13.5}\text{Dy}_{4.8}\text{B}_{7.7}$), the optimum fabricated magnet
has a coercivity of 12 kOe, a remanence of 80 emu/g and
maximum energy product of approximately 15 MGOe.



M_{opt} = Optimum milling time.
 D_{opt} = Optimum powder particle size.
 H_{opt} = Optimum aligning magnetic field strength.
 P_{opt} = Optimum compaction pressure.

A = Find M_{opt}
 B = Optimization of powder using M_{opt}
 C = Optimization of H and P.
 D = Optimization of sintering temperature and time.

Fig. 4.1.1 Schematic illustration of the processes employed for optimization of the final sintered magnets.

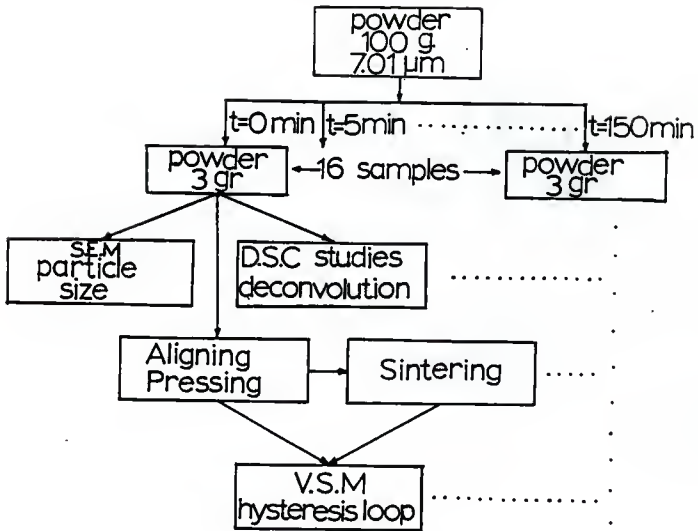


Fig. 4.2.1 Schematic illustration of the processes employed for optimization of the powder particle size.

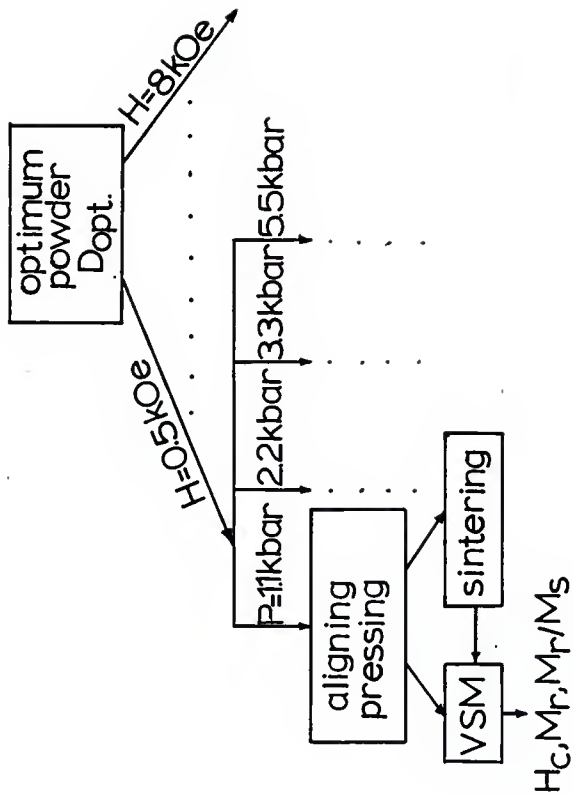


Fig. 4.2.2 Schematic illustration of the processes employed for optimization of the aligning

magnetic field strength, H , and compaction pressure, P .

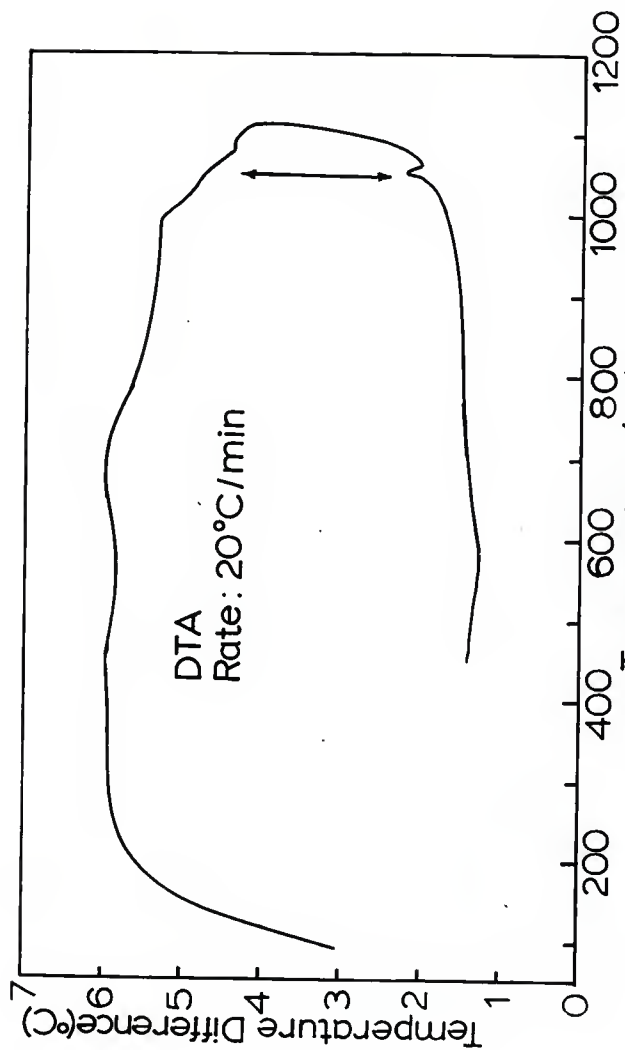


Fig. 4.2.3 Differential thermal analysis (DTA) of $\text{Fe}_{74}\text{Mn}_{13.5}\text{Dy}_{4.8}\text{B}_{7.7}$ as-cast alloy showing a phase transformation at 1040°C (1313 K).

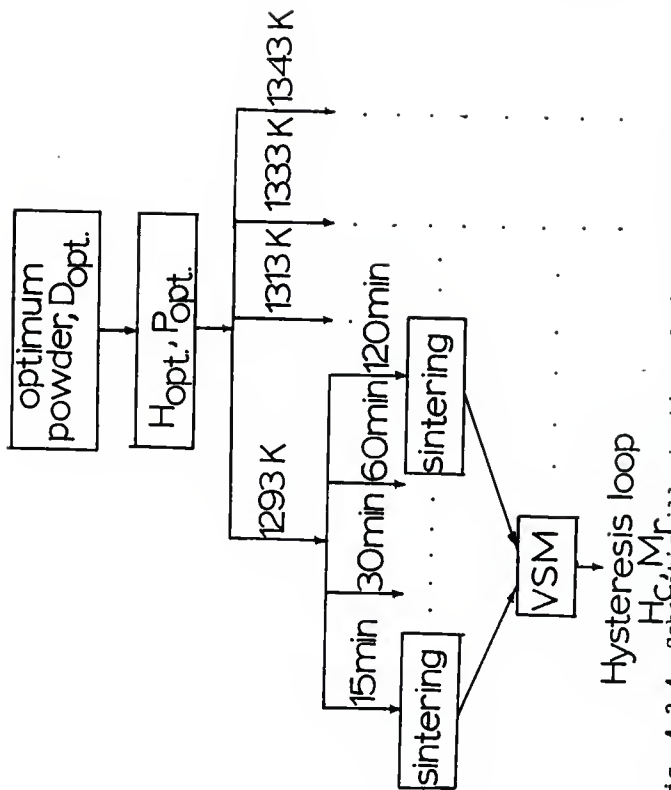


Fig. 4.2.4 Schematic illustration of the processes employed for optimization of the sintering temperature and time.

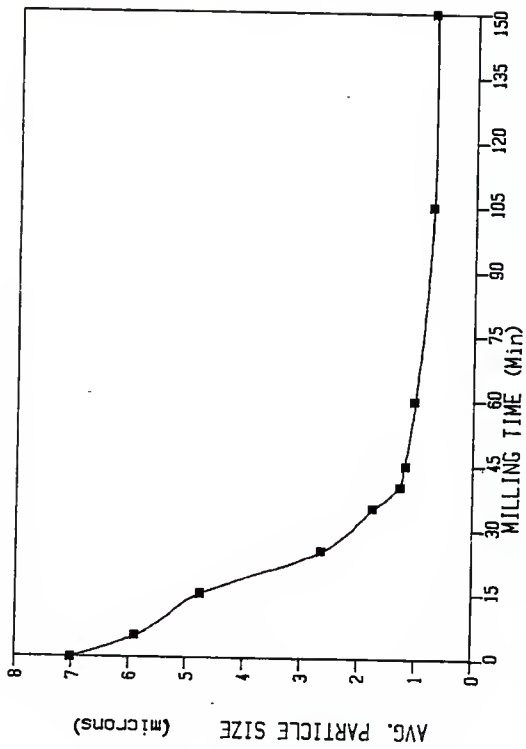


Fig. 4.4.1 Arithmetic average particle size (microns) as a function of milling time (minutes).

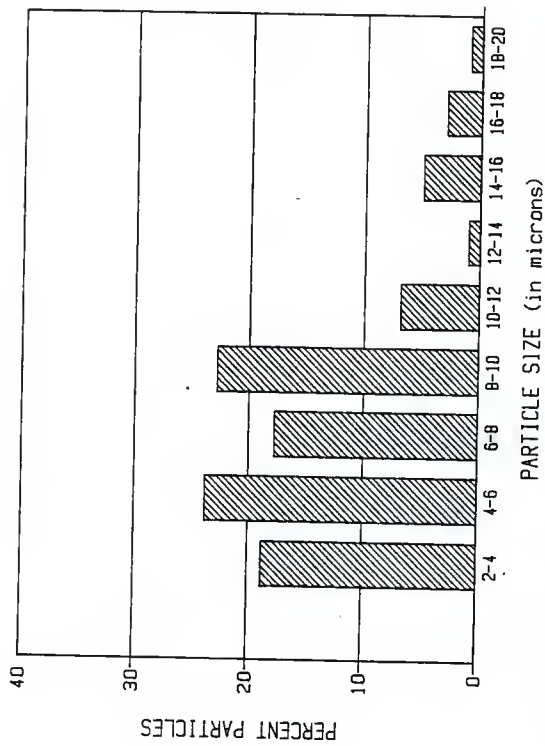


Fig. 4.4.2 Particle size distribution (Percent particles) for a powder milled for zero min. Average diameter=7.01 microns.

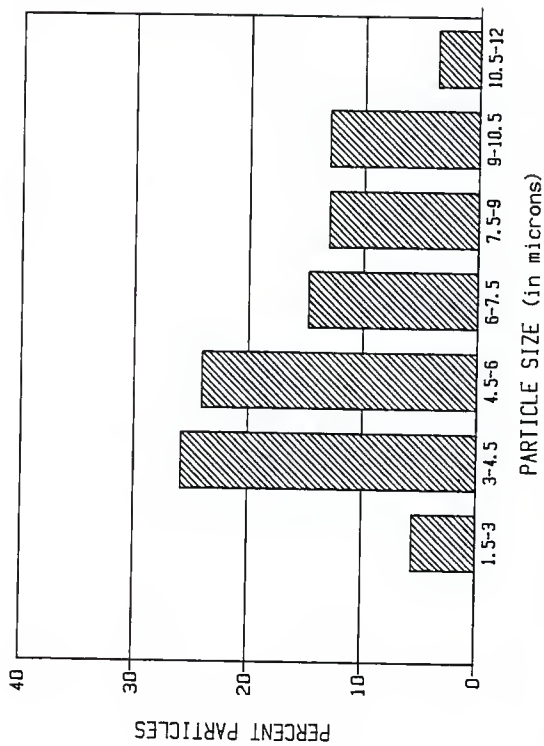


Fig. 4.4.3 Particle size distribution (Percent particles) for a powder milled for 5 min. Average diameter=5.88 microns.

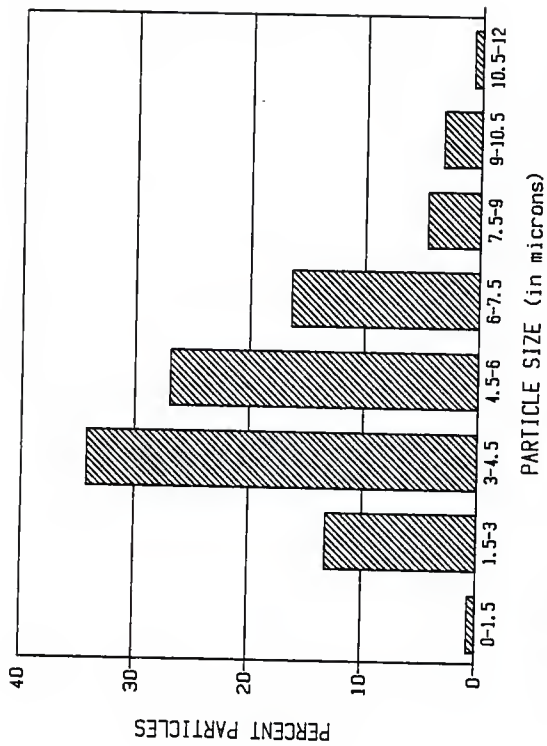


Fig. 4.4.4 Particle size distribution (Percent particles) for a powder milled for 15 min. Average diameter=4.73 microns.

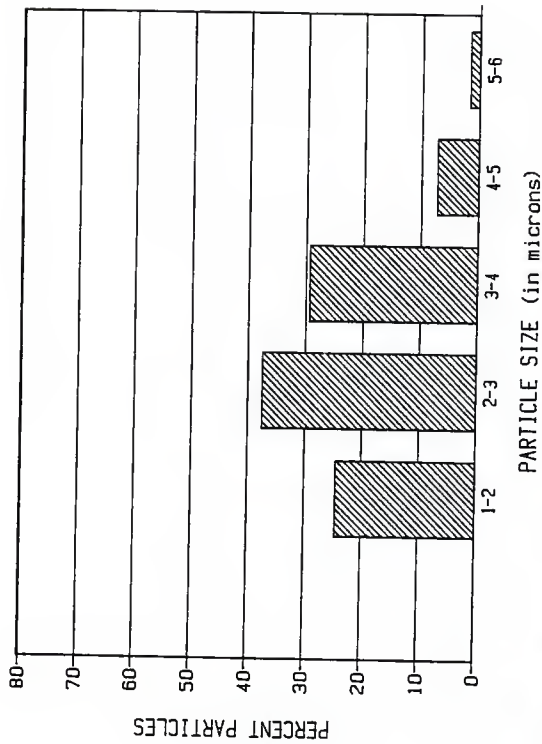


Fig. 4.4.5 Particle size distribution (Percent particles) for a powder milled for 25 min. Average diameter=2.63 microns.

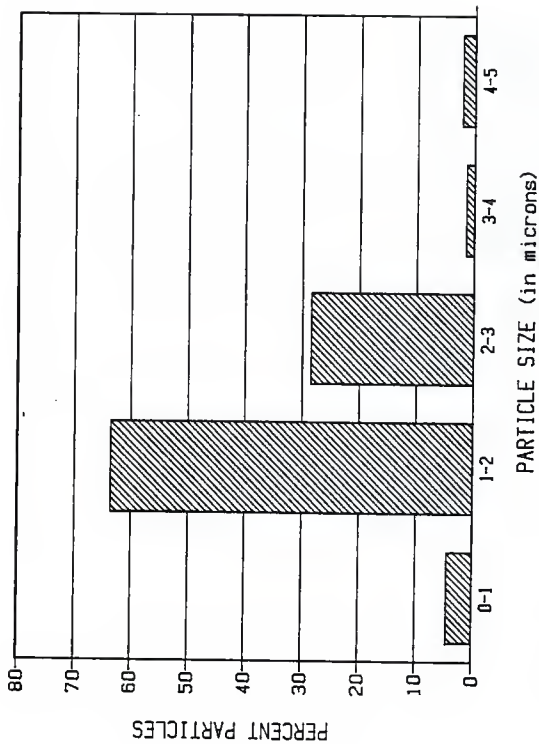


Fig. 4.4.6 Particle size distribution (Percent particles) for a powder milled for 35 min. Average diameter=1.72 microns.

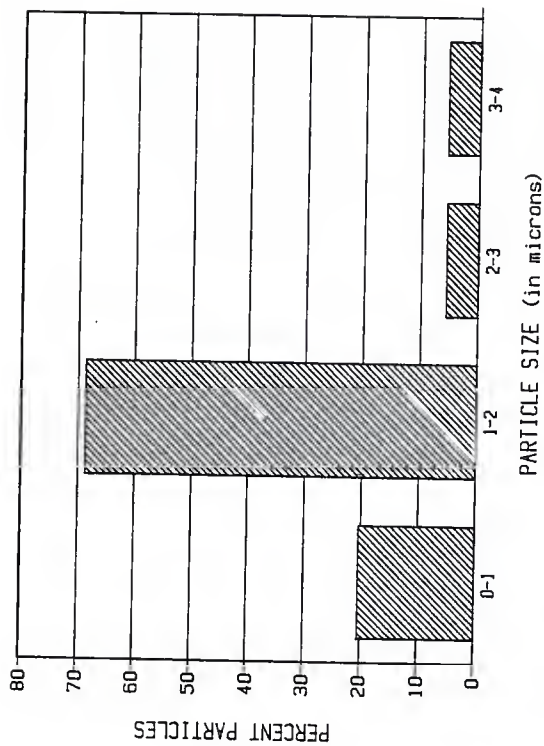


Fig. 4.4.7 Particle size distribution (Percent particles) for a powder milled for 40 min. Average diameter=1.29 microns.

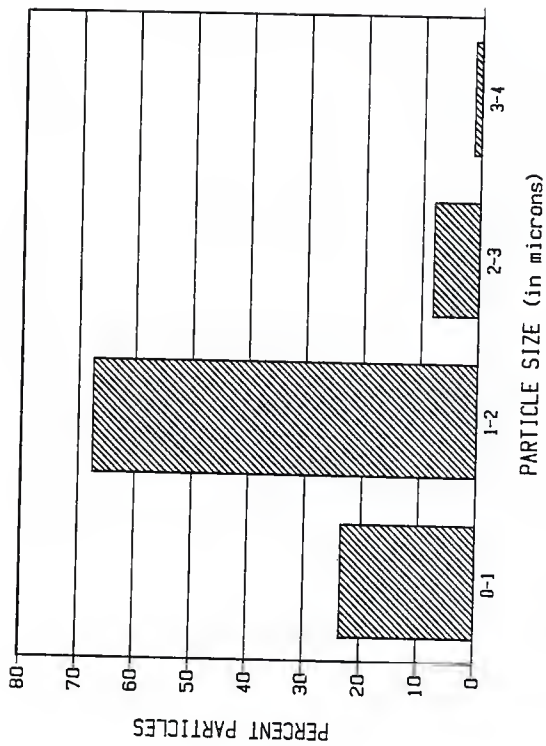


Fig. 4.4.8 Particle size distribution (Percent particles) for a powder milled for 45 min. Average diameter=1.20 microns.

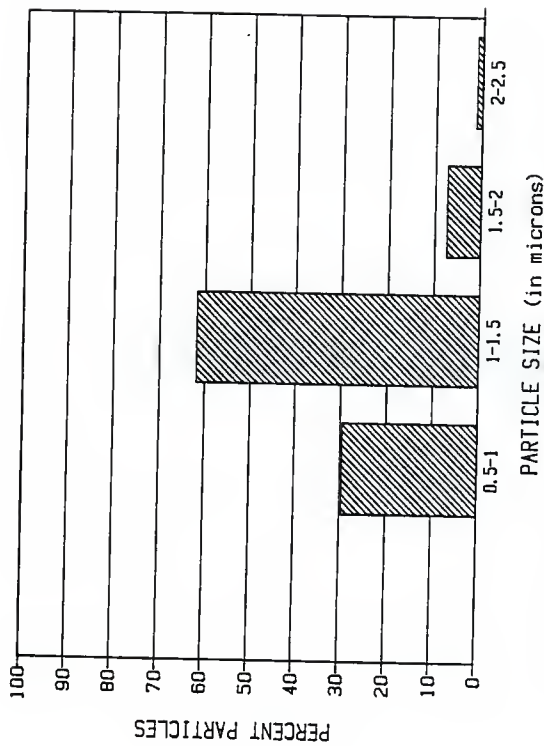


Fig. 4.4.2 Particle size distribution (Percent particles) for a powder milled for 60 min. Average diameter=1.02 microns.

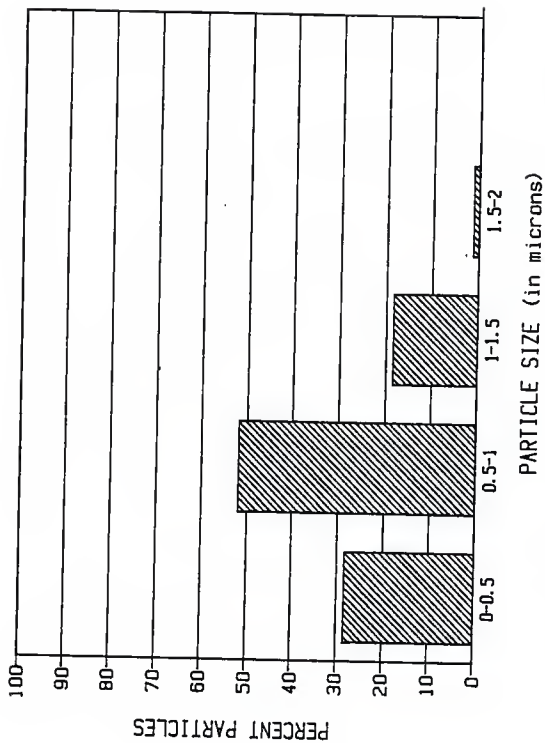


Fig. 4.4.10 Particle size distribution (Percent particles) for a powder milled for 105 min. Average diameter=0.74 microns.

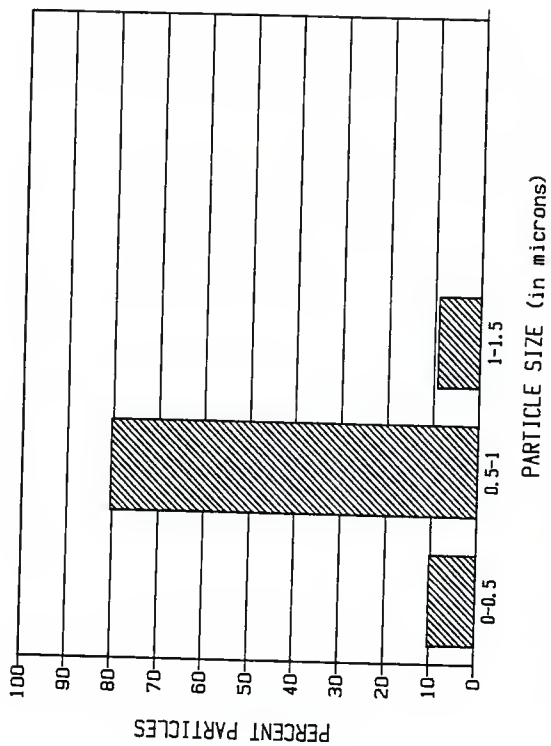


Fig. 4.4.11 Particle size distribution (Percent particles) for a powder milled for 150 min. Average diameter=0.73 microns.

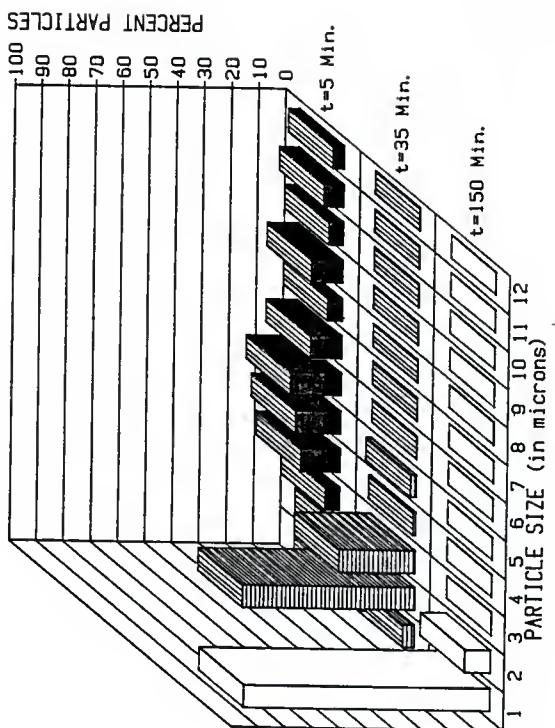


Fig. 4.4.12 Particle size distribution (Percent particles) for a powder milled for 5, 35, 150 min.

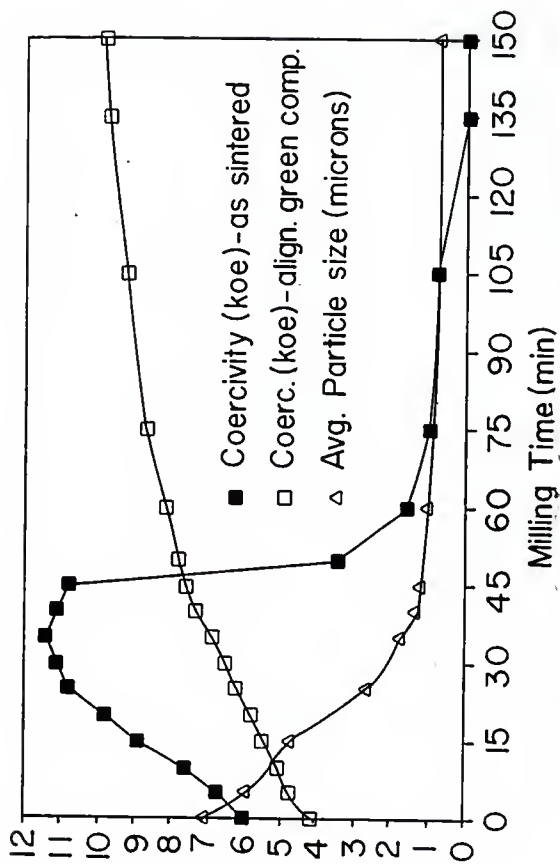


Fig. 4.4.13 Coercivity (koe) of the aligned pressed powders and of the resulting sintered magnets as a function of milling time. The corresponding average particle size (microns) is also shown.

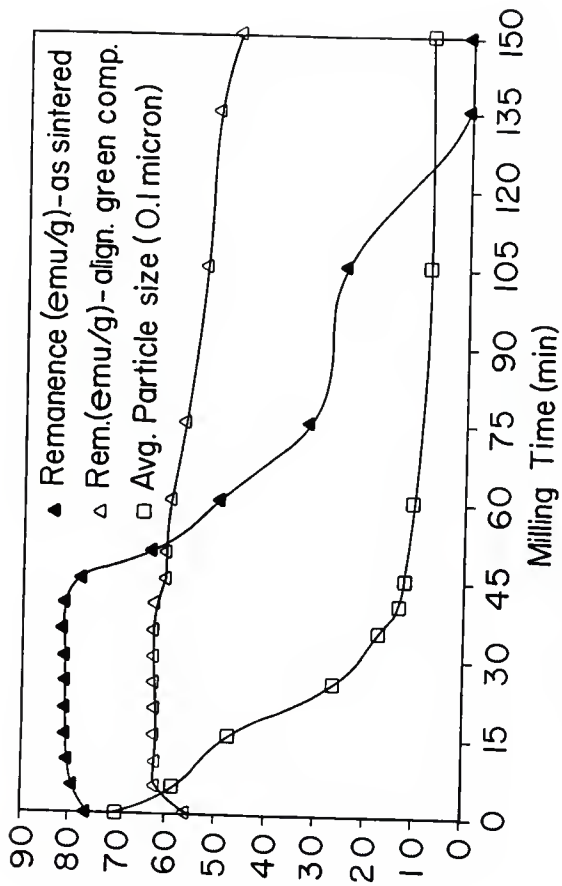


Fig. 4.4.14 Remanence (emu/g) of the aligned pressed powders and resulting sintered magnets as a function of milling time. The corresponding average particle size (in units of 0.1 micron) is also shown.

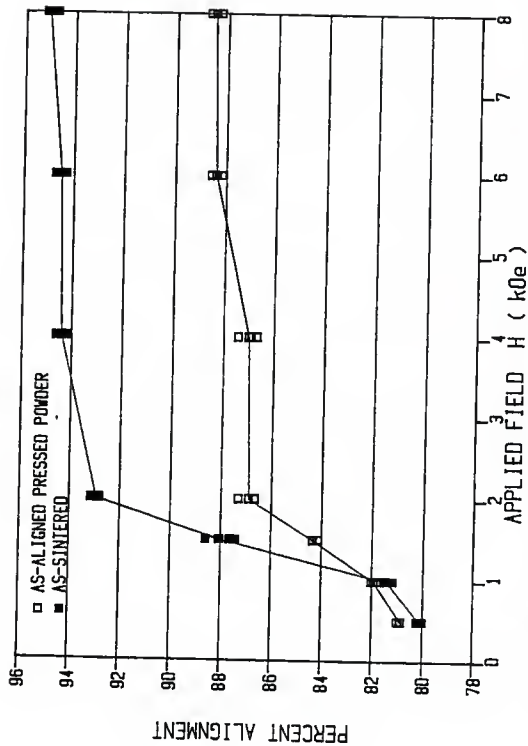


Fig. 4.4.15 Percent alignment (defined as $(M/M_0) \times 100$) of the aligned pressed powder ($D_{avg} = 1.72$ microns) and of the resulting sintered magnets as a function of the aligning magnetic field strength. The compaction pressure is 1.1 kbar. The sintering temperature and time are 1313 K and 15 min, respectively.

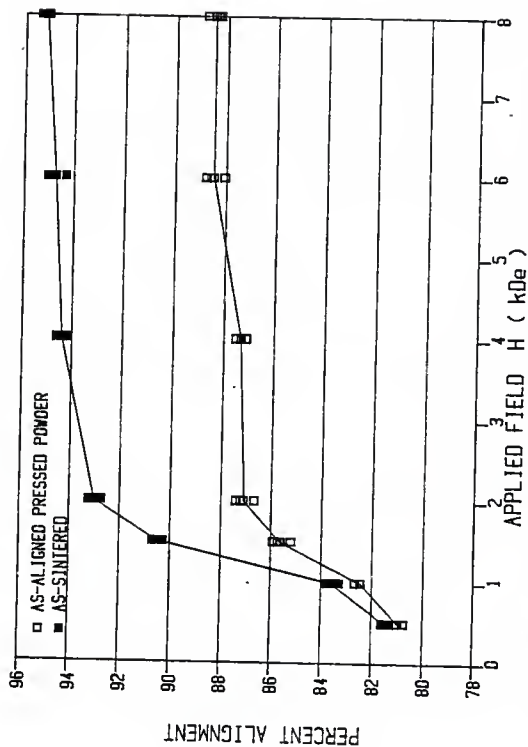


Fig. 4.4.16 Percent alignment (defined as $(M/M_s) \times 100$) of the aligned pressed powder ($D_{avg} = 1.72$ microns) and of the resulting sintered magnet as a function of the aligning magnetic field strength. The compaction pressure is 2.2 kbar. The sintering temperature and time are 1313 K and 15 min, respectively.

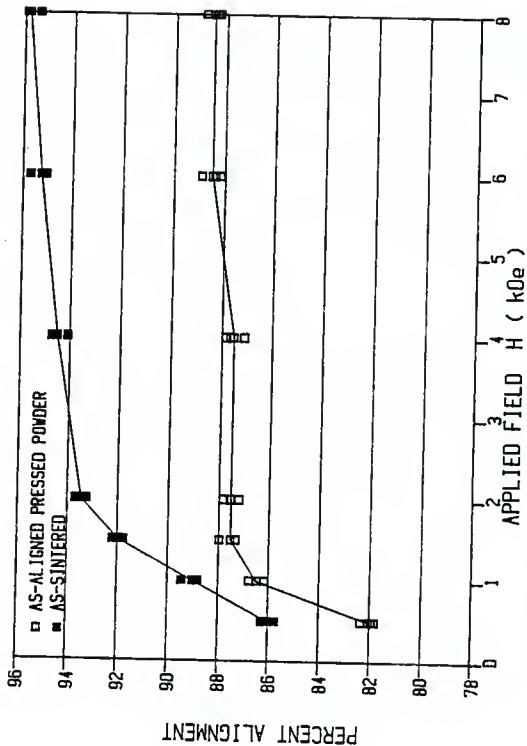


Fig. 4.4.17 Percent alignment (defined as $(M/M_s) \times 100$) of the aligned pressed powder ($D_{avg} = 1.72$ microns) and of the resulting sintered magnets as a function of the aligning magnetic field strength. The compaction pressure is 3.3 kbar. The sintering temperature and time are 1313 K and 15 min, respectively.

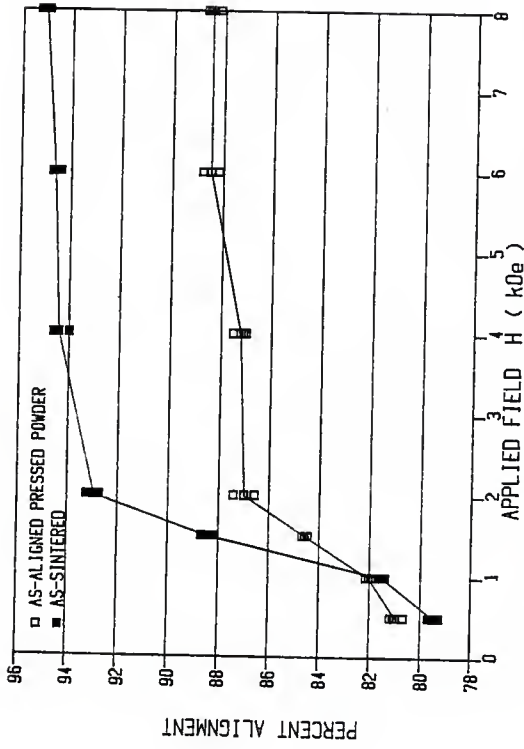


Fig. 4.4.18 Percent alignment (defined as $(M_r/M_s) \times 100$) of the aligned pressed powder ($D_{avg}=1.72$ microns) and of the resulting sintered magnets as a function of the aligning magnetic field strength. The compaction pressure is 5.5 kbar. The sintering temperature and time are 1313 K and 15 min, respectively.

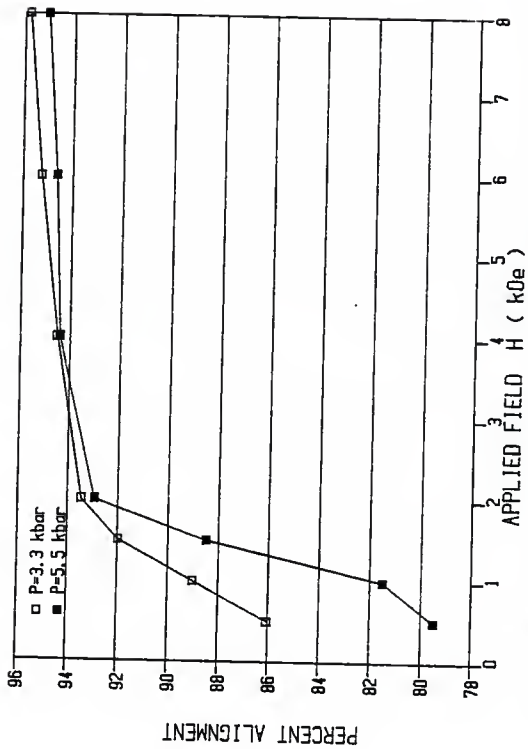


Fig. 4.4.19 Percent alignment (defined as $(M/M_s) \times 100$) of the sintered magnets resulted after pressing the powder (D₅₀ = 1.72 microns) at 3.3 kbar or 5.5 kbar as a function of the aligning magnetic field strength. The sintering temperature and time are 1313 K and 15 min, respectively.

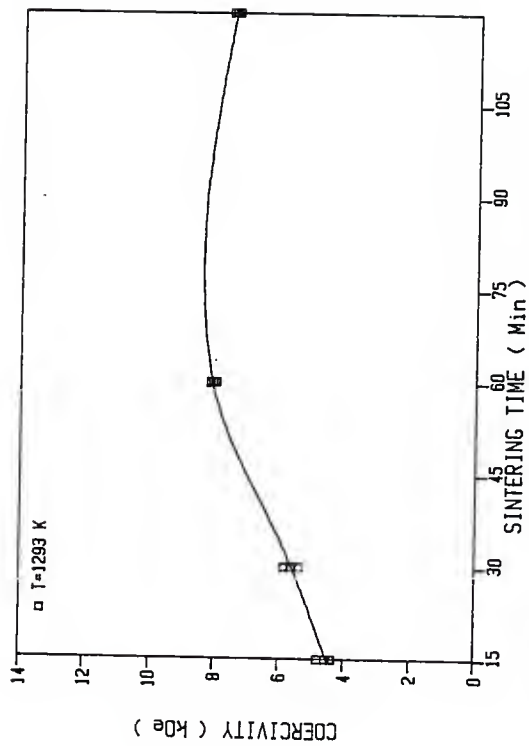


Fig. 4.4.20 Coercivity of magnets sintered at 1293 K as a function of sintering time (minutes).

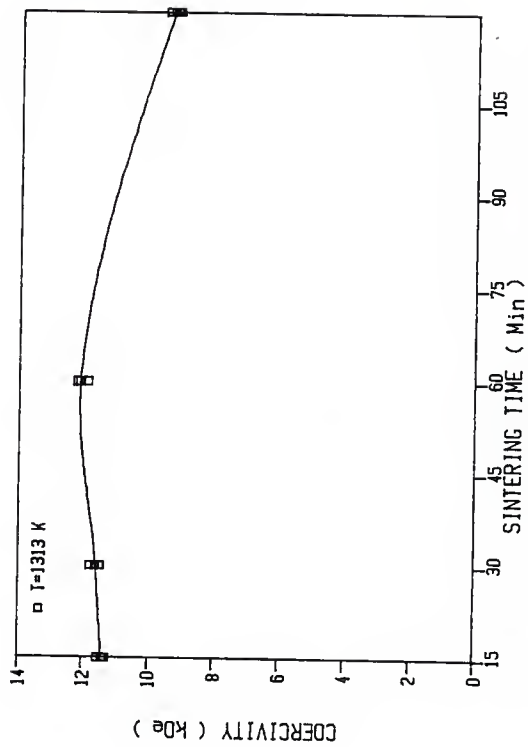


Fig. 4.4.21 Coercivity of magnets sintered at 1313 K as a function of sintering time (minutes).

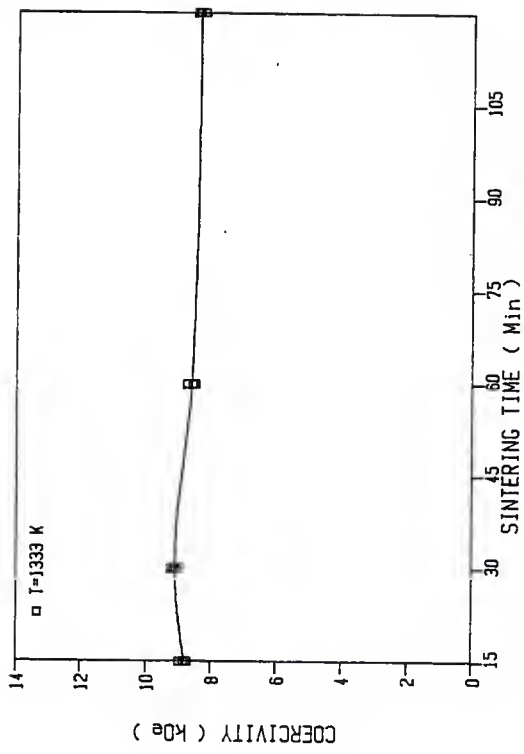


Fig. 4.4.22 Coercivity of magnets sintered at 1333 K as a function of sintering time (minutes).

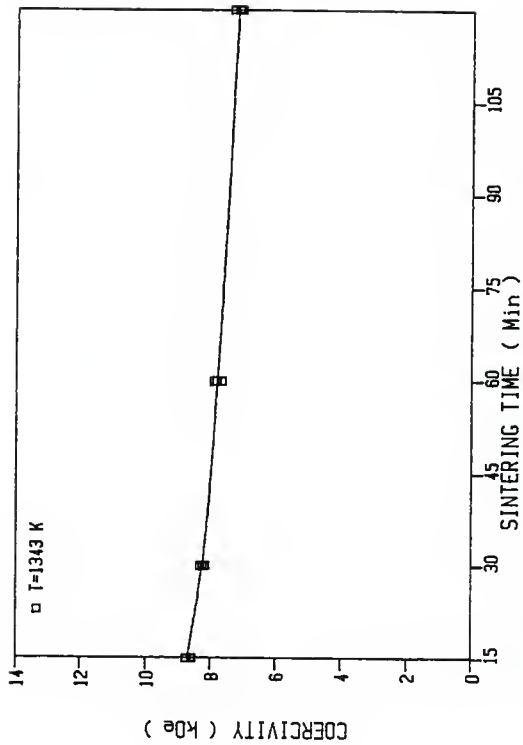


Fig. 4.4.23 Coercivity of magnets sintered at 1343 K as a function of sintering time (minutes).

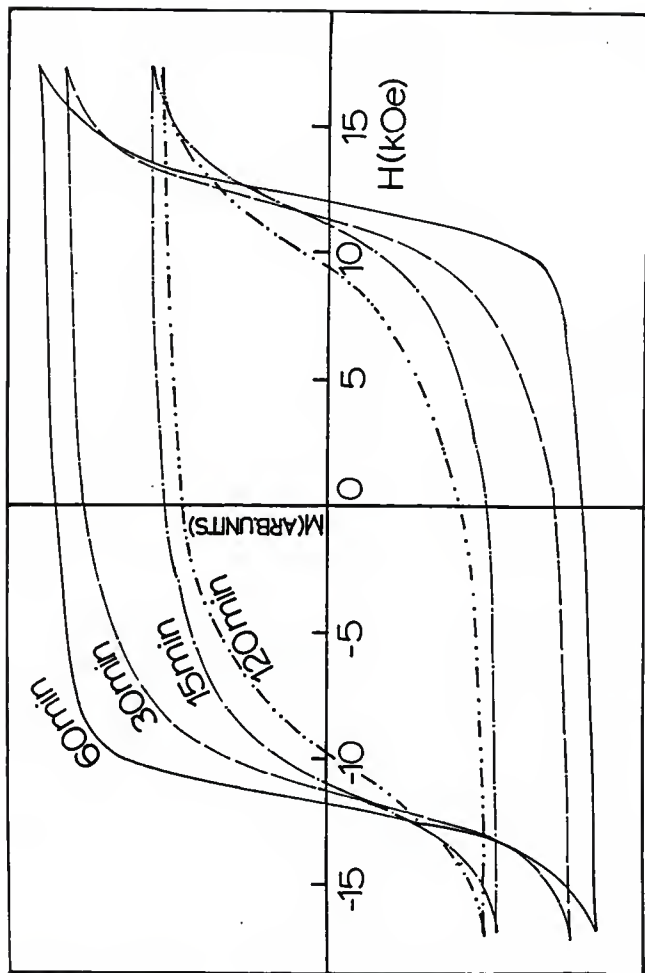


Fig. 4.4.24 Hysteresis loops of magnets sintered at 1313 K for 15, 30, 60 and 120 minutes. The average particle size of the powder used is 1.72 microns. The compaction pressure is 3.3 kbar.

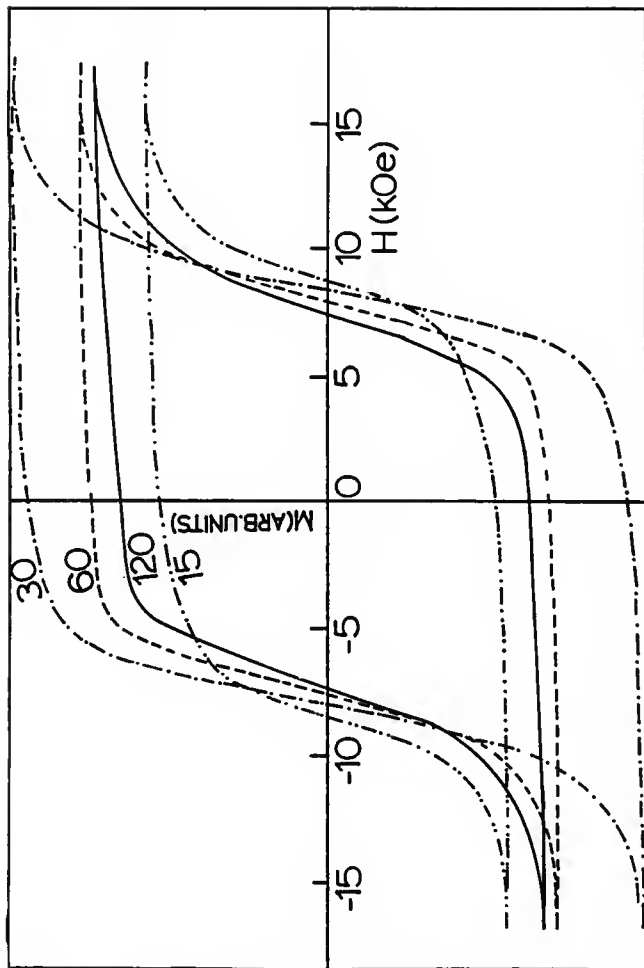


Fig. 4.4.25 Hysteresis loops of magnets sintered at 1343 K for 15, 30, 60 and 120 minutes. The average particle size of the powder used is 1.72 microns. The compaction pressure is 3.3 kbar.

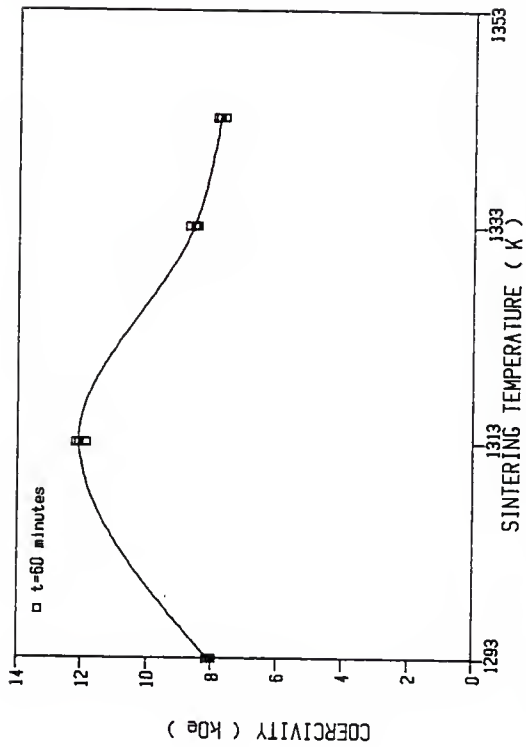


Fig. 4.4.26 Coercivity of magnets sintered for 60 minutes as a function of sintering temperature.

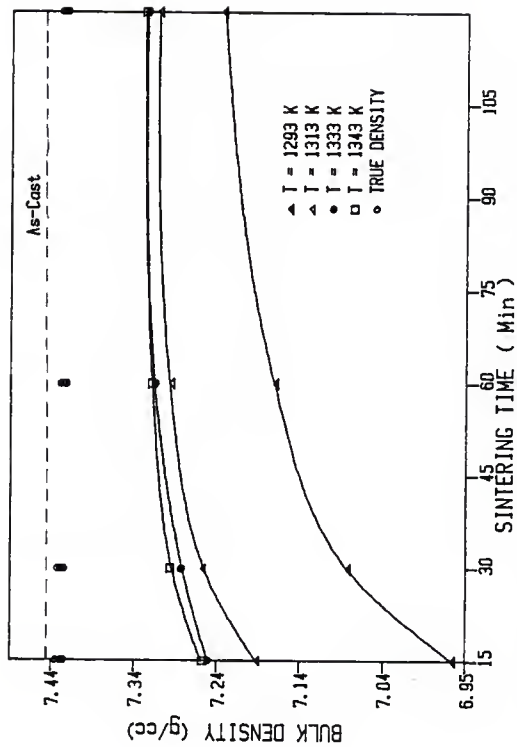


Fig. 4.4.27 Bulk densities (average of three measurements) and true densities as a function of sintering temperature and time. The density of the as-cast alloy is also shown.

Table 4.4.1

Coercivity H_C (in kOe) of $Fe_{74}Mn_{14.5}Dy_{4.8}B_{7.7}$ sintered magnets as a function of sintering temperature T (in K) and time t (in min).

sintering temperature sint. time	1293 K	1313 K	1333 K	1343 K
15 min.	4.75	11.50	8.70	8.75
	4.40	11.40	8.75	8.75
	4.35	11.30	8.95	8.60
	avg.	4.50	11.40	8.80
30 min.	5.85	11.75	9.25	8.35
	5.60	11.60	9.05	8.15
	5.35	11.45	9.00	8.25
	avg.	5.60	11.60	9.10
60 min.	8.15	12.20	8.75	7.90
	8.15	12.20	8.55	7.85
	8.00	11.90	8.50	7.65
	avg.	8.10	12.10	8.60
120 min.	7.60	9.50	8.45	7.35
	7.45	9.15	8.35	7.05
	7.45	9.25	8.40	7.20
	avg.	7.50	9.30	8.40

Table 4.4.2

Bulk densities (in g/cm^3) of $\text{Fe}_{74}\text{Mn}_{13.5}\text{Dy}_{4.8}\text{B}_{7.7}$ sintered magnets as a function of sintering temperature (in K) and time (in min).

sintering temperature sint. time	1293 K	1313 K	1333 K	1343 K
15 min.	6.9643	7.2033	7.2613	7.2642
	6.9665	7.1981	7.2624	7.2614
	6.9663	7.2046	7.2566	7.2802
	avg.	6.9657	7.2020	7.2601
30 min.	7.0961	7.2634	7.2981	7.3075
	7.0911	7.2671	7.2888	7.3013
	7.0912	7.2666	7.2885	7.3045
	avg.	7.0928	7.2657	7.2918
60 min.	7.1835	7.3091	7.3291	7.3301
	7.1783	7.3051	7.3233	7.3261
	7.1815	7.3083	7.3247	7.3299
	avg.	7.1811	7.3075	7.3257
120 min.	7.2453	7.3210	7.3381	7.3362
	7.2491	7.3231	7.3314	7.3395
	7.2493	7.3219	7.3397	7.3383
	avg.	7.2479	7.3220	7.3364

Table 4.4.3

True densities (in g/cm^3) of $\text{Fe}_{74}\text{Mn}_{13.5}\text{Dy}_{4.8}\text{B}_{7.7}$ sintered magnets as a function of sintering temperature (in K) and time (in min).

sintering temperature sint. time	1293 K	1313 K	1333 K	1343 K
15 min.	7.4451	7.4387	7.4371	7.4358
30 min.	7.4417	7.4370	7.4350	7.4340
60 min.	7.4401	7.4351	7.4332	7.4321
120 min.	7.4389	7.4343	7.4321	7.4308

CHAPTER 5

OXIDATION of Fe-R-B POWDERS DURING PROCESSING

5.1 INTRODUCTION

Preparation of sintered permanent magnets from Fe-R-B powders becomes difficult when fine particle size powders are used. It was shown in Section 4.2.1 that there is a drastic decrease in remanence and coercivity of the sintered magnets when the average particle size is less than 1.72 microns (Fig. 4.4.13 and Fig. 4.4.14). Aligned pressed powders do not show this behavior. Therefore, the phenomena which occur during sintering play an important role in the final hard magnetic properties of the final magnet. The literature [33,34] attributes the deterioration of the hard magnetic properties of magnets prepared from fine powders to oxygen contamination.

In the present study DSC measurements were used to examine changes in the $\text{Fe}_{74}\text{Mm}_{13.5}\text{Dy}_{4.8}\text{B}_{7.7}$ powders as a function of temperature. The relationship between the DSC data, powder particle size, and the coercivity and remanence of the aligned pressed powders and resulting sintered magnets have been investigated. The oxygen concentration of the powders has been estimated from the DSC data.

5.2 RESULTS AND DISCUSSION

5.2.1 Differential Scanning Calorimetry (DSC)

In order to better understand the behavior of the magnetic properties of the resulting sintered magnets, DSC data were obtained for the powders of interest as a function of milling time (particle size).

The DSC data for a small solid piece of as-cast alloy were first obtained (Fig. 5.2.1). The smaller surface area of the sample should minimize any effects due to surface reactions. Clearly no exothermic or endothermic peaks are observed in the temperature range between 25-500°C.

The DSC data for all the different particle size powders studied are similar to the one shown in Fig. 5.2.2. The only difference is the amount of heat generated in each case. As the particle size decreases the total heat generated is increased. Comparing the DSC data for as-cast alloy and powders one can conclude that the exothermic peaks obtained for the powders in the region of 50-400°C (Fig. 5.2.2) are due to surface reactions (i.e., oxidation) and not to structural transitions.

Each DSC curve can be explained as the superposition of three exothermic peaks which suggest that three processes are occurring. The most

probable cause of the three different processes is the oxidation reactions of the rare-earths involved in the three phases ($\text{Fe}_{14}\text{R}_2\text{B}$, $\text{Fe}_4\text{R}_1\text{B}_4$ and rare-earth rich phase) present in the as-cast alloy [17,18]. These were identified using optical and electron microscopy and thermomagnetic measurements (to be discussed in Chapter 6). A correlation between the three peaks obtained in the DSC data and the three phases present in the alloy is strongly suggested after deconvolution of the DSC curves.

Deconvoluted DSC curves (based upon a least-squares fit of DSC data) are shown in Fig. 5.2.3, 5.2.4, 5.2.5 and 5.2.6 for average particle sizes 7.01 , 5.33 , 1.72 and 0.91 microns, respectively. The heat corresponding to each of the three peaks as well as the total heat for the different particle size powders is given in Table 5.2.1. These results are also plotted in Fig. 5.2.7. From these data it is obvious that the heat involved in the first process is the most dominant and it increases as the particle size decreases. The second remains almost constant and the third increases slightly to a constant value. The first peak can be attributed to the rare-earth rich phase which is concentrated in the grain boundaries. As the particle size decreases, more of this rare-earth rich phase is exposed. The second peak can be attributed to the $\text{Fe}_4\text{R}_1\text{B}_4$ phase which is present in small

concentrations. As the particle size decreases, its exposed surface remains almost constant. The third peak can be attributed to the $\text{Fe}_{14}\text{R}_2\text{B}$ phase which is the dominant phase. As the milling time increases its exposed surface slightly increases to a constant value. The $\text{Fe}_{14}\text{R}_2\text{B}$ phase is covered with the rare-earth rich phase. This interpretation is also consistent with the fact that the temperature associated with each exothermic peak is directly related to the rare-earth concentration in each phase. A better understanding of the processes occurring with each exothermic peak is needed.

Also the DSC data provide useful information for the temperature at which such phenomena are initiated. For $\text{Fe}_{74}\text{Mn}_{13.5}\text{Dy}_{4.8}\text{B}_{7.7}$, the powders undergo changes at approximately 115°C for coarse powder (7.01 microns), at 90°C for the optimum particle size (1.72 microns) and at around 80°C for the fine powder (0.73 microns).

5.2.2 X-ray Photoelectron Spectroscopy (XPS)

X-ray photoelectron spectroscopy data were obtained for a powder pressed at 4.4 kbar with an average particle size of approximately 1.5 microns. These data show that there are isolated adsorbed oxygen species as well as crystallites of bulk oxides on the surface of the particles. The oxides detected are

Fe_2O_3 , CeO_2 and La_2O_3 . Boron oxides could not be detected in the range of energies investigated. After etching the sample for two to four minutes using argon ions, these same oxides are clearly present. Although isolated adsorbed oxygen species can still be detected, most of the oxygen has been removed by the ion etching.

These XPS preliminary data show clearly that oxygen is present on the powders and may be the reason of the deterioration of the magnetic properties of the resulting sintered magnets.

5.2.3 Estimates of Oxygen Concentration

If it is assumed that the exothermic peaks present in the DSC data are due only to oxidation of the rare-earths, then the oxygen concentrations of the powders can be estimated based upon known heats of reaction. Since the reaction of rare-earth metals with oxygen have very similar heats of reaction and the major rare-earth constituent contained in mischmetal (Mm) is cerium, the reaction between cerium and oxygen is assumed for simplicity. Although the exact stoichiometry of the reaction $\text{Ce} + x (\text{O}) \text{-----} \text{CeO}_x$, ($x=1.75-2$) is not known, the free energy of formation per g atom of oxygen is nearly constant with an average value of 130.45 kcal/g atom of oxygen [35]. The oxygen involved in the reaction, and consequently the oxygen

concentration of the powders, can be estimated knowing the heat generated by the reaction (using the DSC data). The estimated oxygen concentration for different particle size of $\text{Fe}_{74}\text{Mn}_{13.5}\text{Dy}_{4.8}\text{B}_{7.7}$ powders is shown in Table 5.2.2 and plotted in Fig. 5.2.8.

5.2.4 Correlation of DSC and XPS data with hard magnetic properties

In Figure 4.4.14 the remanence of the aligned pressed powders initially increases due to the reduction of the particle size. There are fewer polycrystalline particles and better alignment of the particles [33]. For milling times between 5-35 min (5.88-1.72 microns) the remanence is nearly constant, because the size of the powder approaches the size of single crystal grain. After milling for times longer than 35 min (corresponding to $D_{\text{avg}}=1.72$ microns) the remanence drops from 63 emu/g to 46 emu/g. After sintering (Fig. 4.4.14) a drastic drop of remanence occurred in the same region. The coercivity of the aligned pressed powders increases monotonically as the particle size decreases (Fig. 4.4.13). After sintering the behavior is the same as the remanence. Since sintering is clearly associated with the drastic decreases in remanence and coercivity, oxidation of the powder is the best candidate for the exothermic processes present

in the DSC data. This is strongly suggested also from the XPS data.

The data suggest that sintering, particle size and oxygen concentration are inter-related factors for the development of the hard magnetic properties. It appears that the decrease in remanence and coercivity after sintering corresponds to a critical particle size at which the Fe-R-B crystallites are affected significantly by the formation of bulk oxides. It also appears that, for powder particles larger than the critical particle size (1.72 microns), all the oxygen is present as isolated adsorbed oxygen species. For powder particles smaller than the critical particle size the oxygen is present as isolated adsorbed oxygen and as crystallites of bulk oxides. This has been confirmed by X-ray photoelectron spectroscopy.

5.2.5 Application to Processing

For the $\text{Fe}_{74}\text{Mn}_{13.5}\text{Dy}_{4.8}\text{B}_{7.7}$ alloy, the critical particle size is 1.72 microns and the corresponding critical oxygen concentration is 0.428 wt%. This information concerning the critical oxygen concentration can be very useful in general for process control prior to sintering. Powders having different oxygen concentrations can be blended in such way so that the total oxygen concentration is below the critical value.

Figure 5.2.9 shows the result of blending of two powders with oxygen concentrations 0.45 wt% and 0.37 wt%, respectively, in such way that the total oxygen concentration was 0.41 wt%. The first powder (0.45 wt% oxygen) yielded sintered magnets with a coercivity of 3.5 kOe and a remanence of 63 emu/g. The second powder (0.37 wt% oxygen) yielded sintered magnets with a coercivity of 10.8 kOe and a remanence of 80 emu/g. The resulted powder mixture (0.42 wt%) yielded sintered magnets with a coercivity of 10.5 kOe and remanence of 80 emu/g (Fig. 5.2.9).

5.3 CONCLUSIONS

1) Three exothermic processes are taking place in the powders upon heating in the temperature range 50-400°C. These processes seem to affect dramatically the hard magnetic properties of the resulting sintered magnets after a critical particle size. The most probable explanation of these exothermic processes is the oxidation of the rare-earth metals involved in the three phases present in the as-cast alloy.

2) X-ray photoelectron spectroscopy confirms the presence of two forms of oxygen on the surface of the powder.

3) For all the systems studied there is a critical oxygen concentration associated with a critical particle size which limits the development of the hard magnetic properties of the sintered magnets. For the alloy under investigation the critical particle size is 1.72 microns and the associated oxygen concentration is 0.428 wt% .

4) The information about the critical oxygen concentration can be used successfully for process control prior to sintering by blending powders with different oxygen concentration in such way that the total oxygen concentration is kept below the critical value.

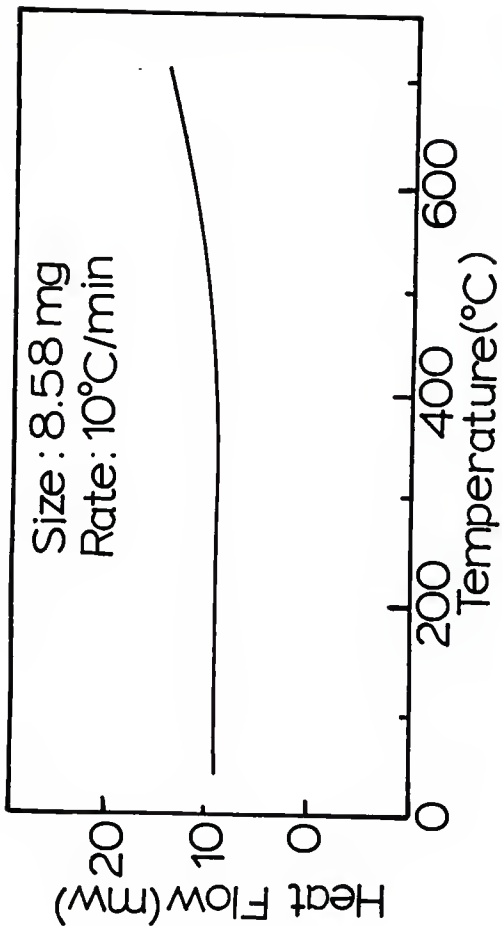


Fig. 5.2.1 Differential scanning calorimetry (DSC) data for a solid piece of as-cast alloy with composition $\text{Fe}_{74}\text{Mn}_{13.5}\text{DY}_{4.8}\text{B}_{7.7}$.

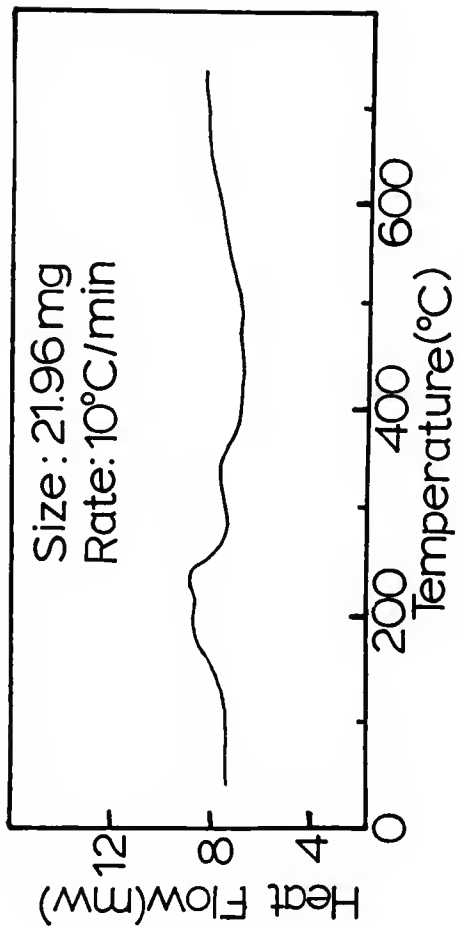


Fig. 5.2.2 DSC data for Fe₇₄Mn_{13.5}DY_{4.8}B_{7.7} powder with average particle size 7.01 microns.

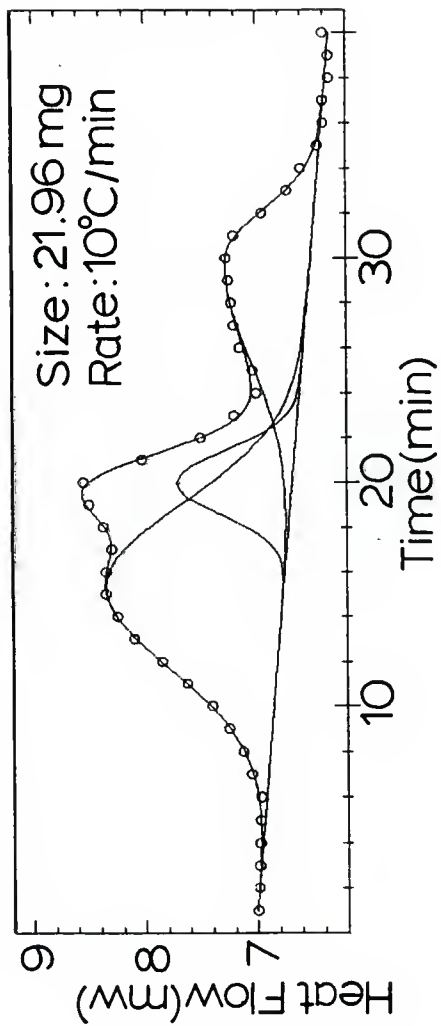


Fig. 5.2.3 Deconvoluted DSC curve of $\text{Fe}_{74}\text{Mn}_{13.5}\text{DY}_{4.8}\text{B}_{7.7}$ powder with an average particle size of 7.01 microns.

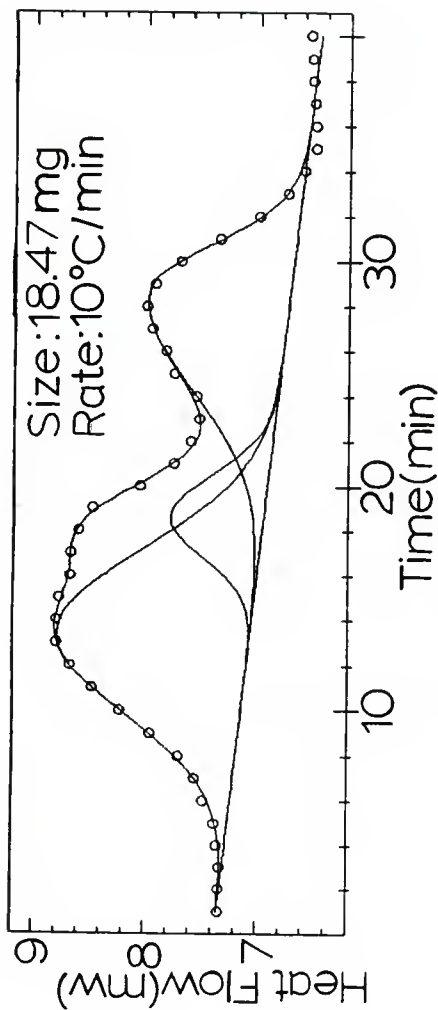


Fig. 5.2.4 Deconvoluted DSC curve of $\text{Fe}_{74}\text{Mn}_{13.5}\text{Dy}_{4.8}\text{B}_{7.7}$ powder with an average particle size of 5.33 microns.

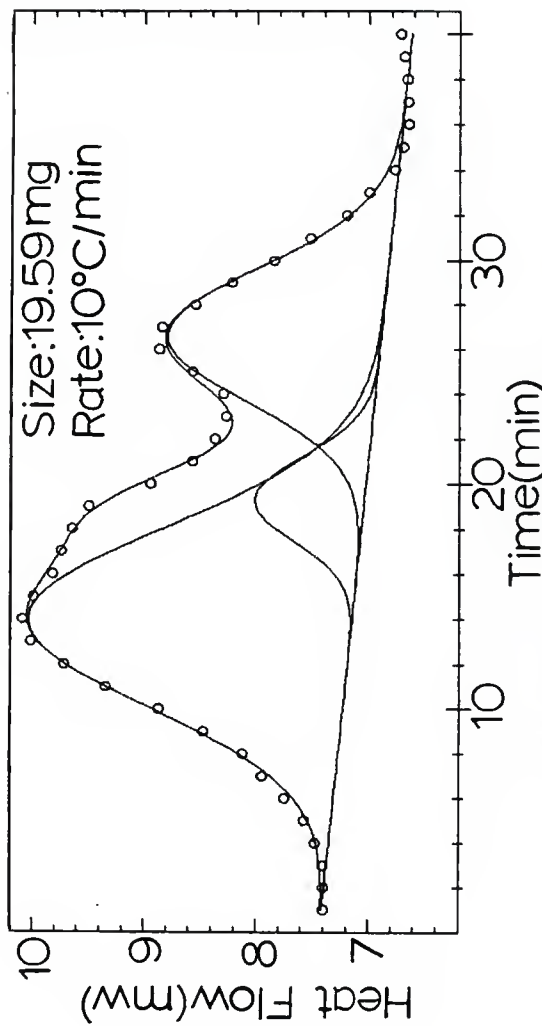


Fig. 5.2.5 Deconvoluted DSC curve of $\text{Fe}_{74}\text{Mm}_{13.5}\text{Dy}_{4.8}\text{B}_{7.7}$ powder with an average particle size of 1.72 microns.

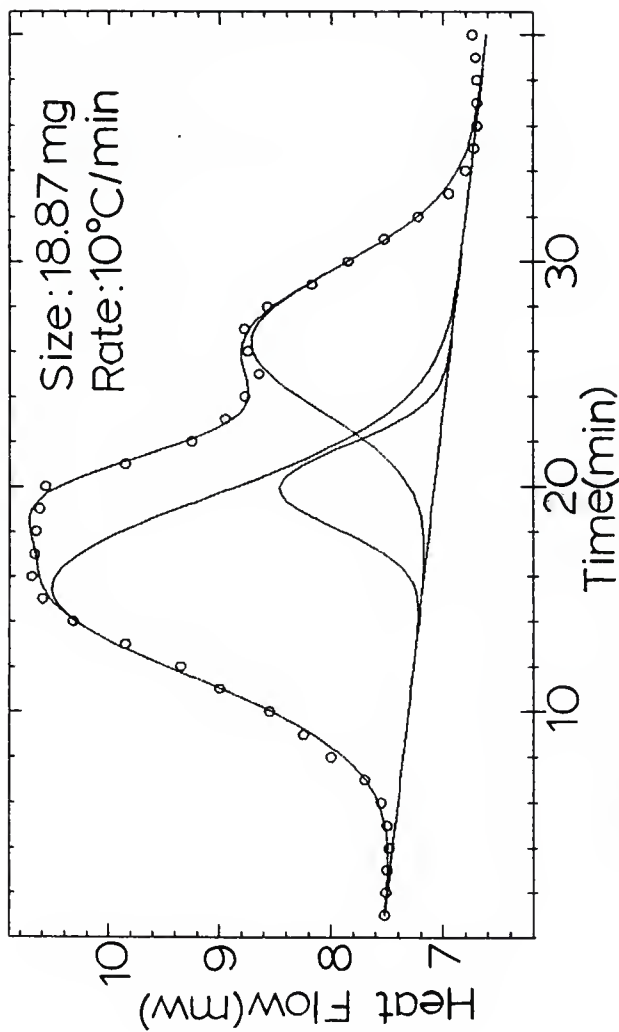


Fig. 5.2.16 Deconvoluted DSC curve of Fe₇₄Mm_{13.5}DY_{4.8}B_{7.7} powder with an average particle size of 0.91 microns.

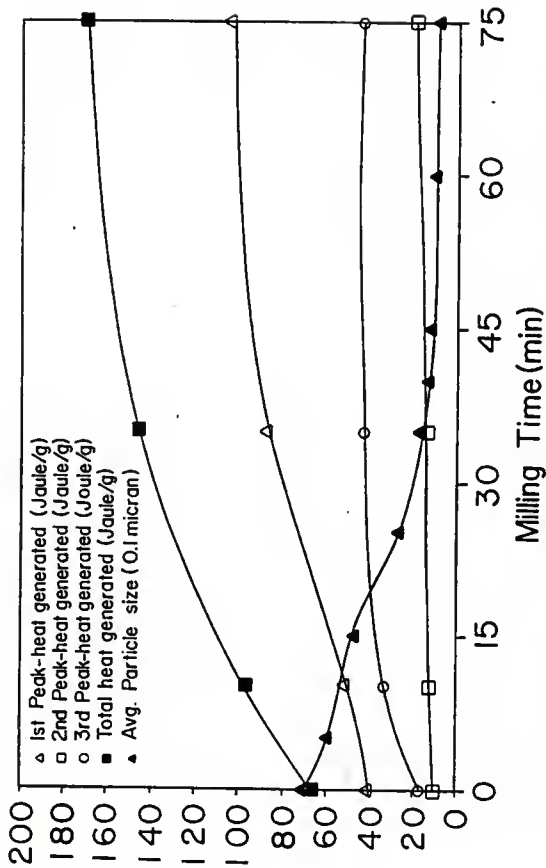


Fig. 5.2.7 Heats corresponding to each of the three peaks and total heat as a function of milling time (particle size in units of 0.1 microns).

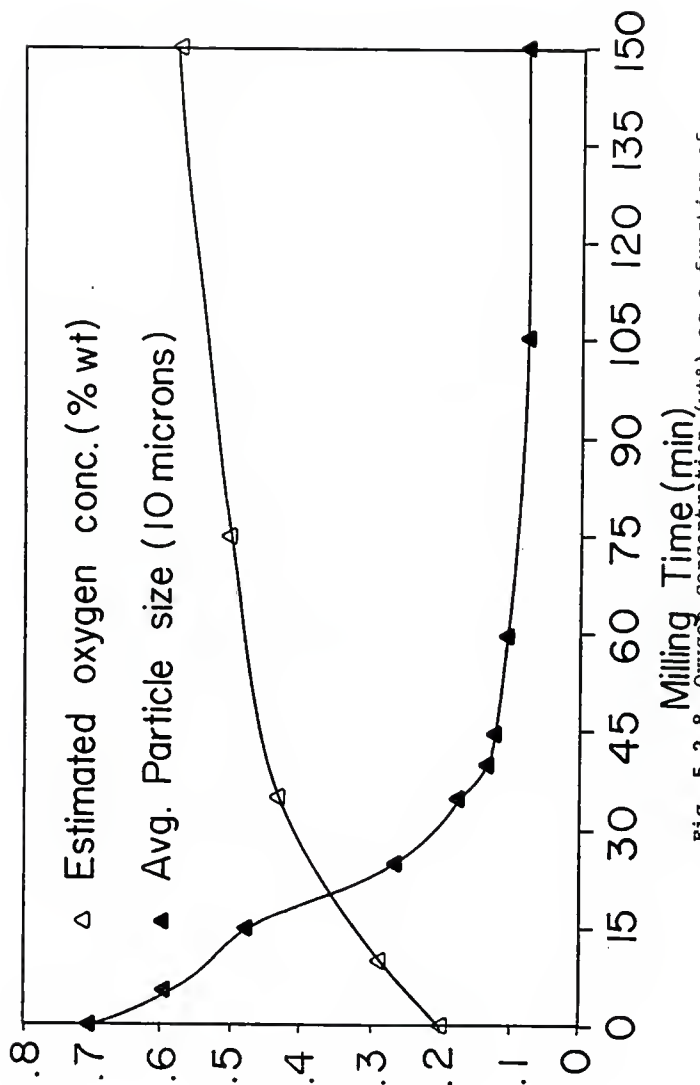


Fig. 5.2.8 Oxygen concentration (wt%) as a function of milling time (particle size in units of 10 microns).

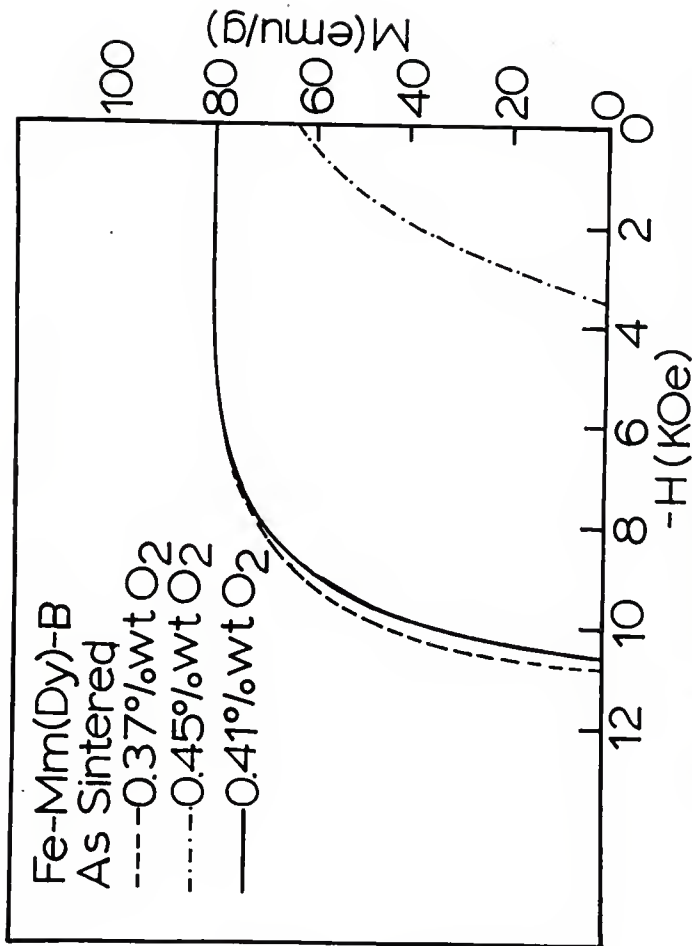


Fig. 5.2.9 Demagnetization curves of sintered magnets prepared using powders with different oxygen concentrations.

Table 5.2.1

Heats (in Joule/g) corresponding to each of three peaks and total heat as a function of milling time (in min) and average particle size (in microns) of the powder.

Milling time (min)	Average particle size (microns)	1st peak (Joule/g)	2nd peak (Joule/g)	3rd peak (Joule/g)	total (Joule/g)
0	7.01	40.02	9.92	17.25	67.19
10	5.33	51.02	12.51	33.44	96.97
35	1.72	88.05	14.08	43.79	145.92
75	0.91	104.50	20.19	46.01	170.70

Table 5.2.2

Oxygen concentration (in wt%) as a function of milling time (in min) and average particle size (in microns) of the powder.

Milling time (min)	Average particle size (microns)	Oxygen concentration (weight %)
0	7.01	0.197
10	5.33	0.284
35	1.72	0.428
75	0.91	0.500
150	0.73	0.572

CHAPTER 6

HARD MAGNETIC PROPERTIES—THE ORIGIN OF HYSTERESIS

6.1 INTRODUCTION

The origin of hysteresis is difficult to explain. For most of the existing hard magnetic materials the origin of hysteresis has been explained using the models of nucleation of reversed domains and domain wall pinning [36,37,38,39,40,41,42,46,47,49].

Thermomagnetic measurements, optical and electron microscopy, and measurements of the magnetic properties as a function of the applied field were employed in this study to understand the origin of hysteresis for the magnets prepared. The information taken from these data, like coercivity as a function of temperature and applied field, the microstructure and magnetic domains, are very useful in interpreting the origin of hysteresis. The details of the experimental techniques have been described in Sections 3.2.4 and 3.2.6.

6.2 RESULTS OF THERMOMAGNETIC MEASUREMENTS

6.2.1 Curie Temperature

This experiment was done using a high temperature VSM. The magnetization versus temperature is plotted in the presence of a small magnetic field (1 kOe). The Curie temperature is defined as the temperature where the magnetization becomes zero. Figure 6.2.1 shows the magnetization versus temperature of the $\text{Fe}_{74}\text{Mm}_{13.5}\text{Dy}_{4.8}\text{B}_{7.7}$ as-cast alloy. The two inflection points (two Curie temperatures) indicate the presence of two different phases in the alloy. The corresponding Curie temperature are 265°C and 290°C , respectively. The sintered magnets show exactly the same behavior.

6.2.2 Coercivity and Remanence as a Function of Temperature.

The hysteresis loops (Fig. 6.2.2) of the sintered magnet as a function of temperature were obtained. The values of coercivity and remanence as a function of temperature are given in Table 6.2.1 and plotted in Figures 6.2.3 and 6.2.4, respectively. Both, coercivity and remanence were found to decrease with increasing the temperature.

6.3 RESULTS FROM MICROSTRUCTURAL ANALYSIS

The microstructure is probably the most important information that one can use to explain the origin of hysteresis [36,37,38,39,40,41,42]. In the present study both optical and electron microscopy were employed.

6.3.1 Optical Microscopy

Figure 6.3.1 shows the grain structure of the optimum fabricated $\text{Fe}_{7.4}\text{Mm}_{13.5}\text{Dy}_{4.8}\text{B}_{7.7}$ sintered magnet. From this picture one can clearly see the presence of at least two phases. The white grains are the $\text{Fe}_{14}\text{R}_2\text{B}$ phase and the gray grains are the rare-earth rich phase. This was confirmed using energy dispersive X-ray analysis (Section 6.3.2).

6.3.2 Electron Microscopy

Figure 6.3.2 shows micrographs obtained regarding the microstructure of the optimum fabricated sintered magnet. Picture 6.3.2(a) shows the microstructure of an unetched sample. In the unetched sample one can see the main $\text{Fe}_{14}\text{R}_2\text{B}$ phase (A) and the rare-earth rich phase (B) distributed mostly in the grain boundaries of A phase. The $\text{Fe}_{14}\text{R}_2\text{B}$ phase (A) and rare-earth rich phase (B) were identified using energy dispersive X-ray analysis. Typical spectra of the A and B regions are shown in Fig. 6.3.3 and 6.3.4, respectively.

The chemical analysis of these regions is given in Table 6.3.1. This analysis is based on Fe and rare-earth components since boron cannot be detected by this method. The A region has a composition of approximately 87.02 mole% Fe and 12.98 mole% rare-earth which is very close to the Fe/rare-earth ratio of the $Fe_{14}R_2B$ phase. The distribution of the rare-earths involved in this phase is 6.72 mole% Dy, 2.19 mole% (Nd and Pr) and 4.07 mole% (Ce and La). The B region shows a composition of 44.35 mole% rare-earth and 55.65 mole% Fe. The distribution of rare-earths involved in this phase is 2.74 mole% Dy, 5.05 mole% (Nd and Pr) and 36.57 mole% (Ce and La). In the unetched sample, no $Fe_4R_1B_4$ phase could be detected because it was invisible.

Picture 6.3.2(b) shows the microstructure of the same sintered sample after etching a few seconds with 3% nital. The $Fe_{14}R_2B$ phase (A) were found to be the large grains (3-6 microns). They appear as the dark phase in these micrographs. The rare-earth rich phase (B) was located in the grain boundaries around the A phase and especially in the black regions shown in the micrograph. A small grain size white phase was now very visible. A typical analysis of the grains (noted as C in the picture) is 80.26 mole% Fe and 19.74 mole% rare-earths (Table 6.3.1), which is in agreement with the composition of a $Fe_4R_1B_4$ phase.

The corresponding energy dispersive X-ray spectra is shown in Fig. 6.3.5.

A closer look of the $\text{Fe}_{14}\text{R}_2\text{B}$ phase shows that the grains are surrounded by inclusions, which could not be identified. Figure 6.3.6 shows a picture of a $\text{Fe}_{14}\text{R}_2\text{B}$ grain contaminated with such inclusions. The size of these inclusions is approximately 0.3 microns and these could possibly be oxides. The importance of the presence of such inclusions with respect to the magnetic hysteresis of the sintered magnet will be discussed in Section 6.5.

6.4 RESULTS OF MEASURING MAGNETIC PROPERTIES AS A FUNCTION OF APPLIED FIELD

A study of the coercivity and remanence as a function of the applied field can give important information about the origin of hysteresis [50]. The initial magnetization curves (Section 2.2) can give information about the origin of hysteresis as well. These measurements were obtained on samples with the following two different starting magnetic states.

- (i) on thermally demagnetized samples and,
- (ii) on fully magnetized samples.

i) **Thermally demagnetized samples:**

The samples were first put in an applied field which was increased from zero to the desired field strength. Then the demagnetization curves were obtained as shown in Fig. 6.4.1.

ii) **Fully magnetized samples:**

The sample was first fully magnetized with the maximum available forward magnetic field (17 kOe) and then demagnetized by reducing the amplitude of the applied field (ac demagnetized). Then the ac demagnetized sample was ac magnetized by increasing the amplitude of the applied field as shown in Figure 6.4.2.

6.4.1 Field Dependence of Coercivity and Remanence

The field dependence of coercivity of a thermally demagnetized (case (i)) and ac demagnetized sample (case (ii)) are shown in Figure 6.4.3. In the case of the thermally demagnetized sample the coercivity increases slowly up to an applied field of 4 kOe. Then it increases rapidly to a saturation value. In the case of the fully magnetized sample (ac demagnetized) the coercivity remains zero up to a threshold magnetic field of 7.6 kOe where it increases dramatically. The same behavior (Fig. 6.4.4) was obtained in each case for the remanence.

6.4.2 Initial Magnetization Curves

The initial magnetization curves for the thermally demagnetized and ac demagnetized samples are shown in Figures 6.4.1 and 6.4.2, respectively. In the first case the initial magnetization increases sharply to saturation. In the second case the initial magnetization increases slowly up to a critical field (7.60 kOe) and then increases sharply to saturation. Figure 6.4.5 shows the magnetization curves for both cases for comparison.

6.4.3 Magnetic Domains

Figures 6.4.6 shows magnetic domains obtained on a thermally demagnetized sintered sample. The size of the domains is around 0.4 microns which is very close to the value obtained by others [51] for Fe-Nd-B sintered magnets.

6.5 DISCUSSION-CONCLUSIONS

The Curie temperature is found to be 290°C which is slightly less than that for Fe-Nd-B sintered magnets (310°C) [43]. The reason of the presence of the light rare-earths Ce and La which are involved in the $\text{Fe}_{14}\text{R}_2\text{B}$ phase. The temperature dependence of coercivity and remanence shows a decrease of 52% and 17% at 125°C , respectively. These values are higher than the Nd-based magnets [52].

The initial magnetization curves for a thermally and ac demagnetized sample are shown in Figure 6.4.5. It is obvious that in the thermally demagnetized samples the domain walls move freely inside the grains resulting in a drastic increase of magnetization at relatively low fields. However, when the samples are ac demagnetized, after they were initially fully magnetized, the "effective initial" curve (Fig. 6.4.5) differs. It lies below that of the thermally demagnetized sample. This is an indication that after the application of the magnetic field the domain wall distribution changes and some of the walls are engaged with different and stronger pinning sites opposing the complete saturation of the sample [50,53]. It is interesting to note that there is a threshold field (critical field) for which the magnetization increases drastically. The value of threshold field is very close

to the coercivity and it appears to give the appropriate energy to release the domain walls from their interaction with the high energy pinning sites. This is also suggested by the field dependence of coercivity (Fig. 6.4.3).

The coercivity has a zero value up to a certain applied magnetic field (which is equal to the threshold field) and then increases drastically. The magnitude of this effect is characteristic of uniform domain wall pinning [53], typical of that observed in $\text{Sm}_2(\text{Co,Fe,Cu,Zr})_{17}$ alloys [54].

The microstructure shown in Figure 6.3.6 shows clearly that the grains are surrounded by inclusions. It is very possible that the inclusions found inside the grains provide the high energy pinning sites which result in the observed magnetic properties. Therefore, it appears that at the thermally demagnetized state the domain walls move easily with possible domain wall pinning at the grain boundaries. After the samples are subjected to an ac field a situation is reached which strongly resembles uniform domain wall pinning.

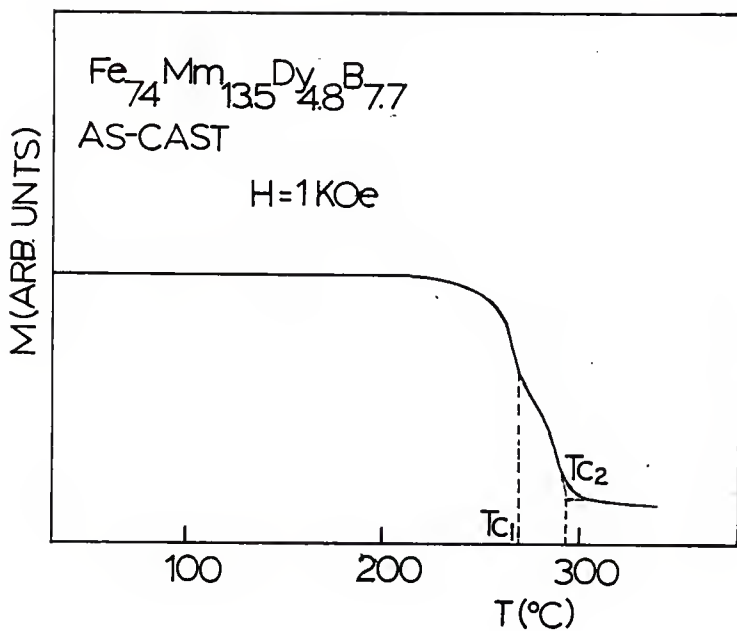


Fig. 6.2.1 Magnetization versus temperature of an $\text{Fe}_{74}\text{Mm}_{13.5}\text{Dy}_{4.8}\text{B}_{7.7}$ as-cast alloy. The first Curie temperature T_{C1} is 265°C and the second T_{C2} is 290°C .

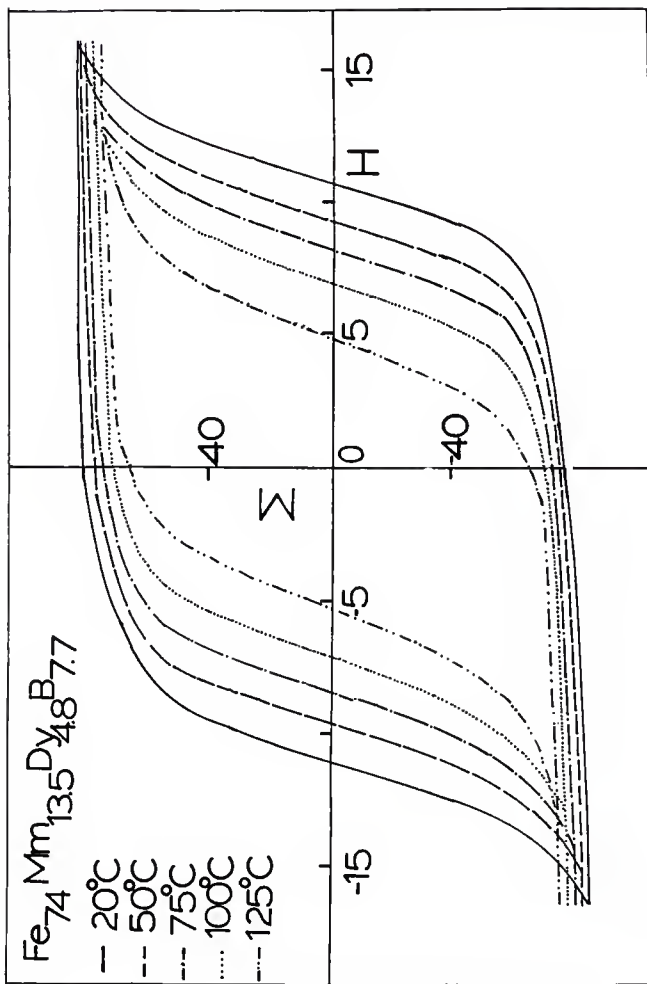


Fig. 6.2.2 Hysteresis loops of $\text{Fe}_{74}\text{Mm}_{13.5}\text{Dy}_{4.8}\text{B}_{7.7}$ sintered magnet as a function of temperature.

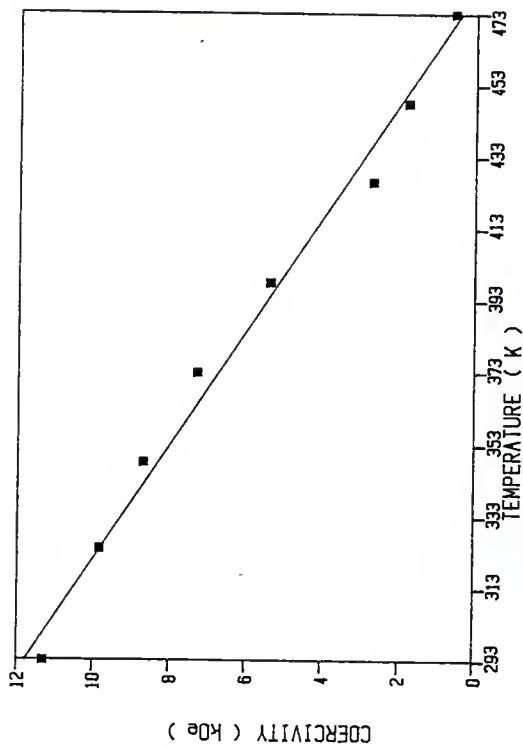


Fig. 6.2.2.3 Coercivity (kOe) of $\text{Fe}_{74}\text{Mn}_{13.5}\text{Dy}_{4.8}\text{B}_{7.7}$ sintered magnet as a function of temperature.

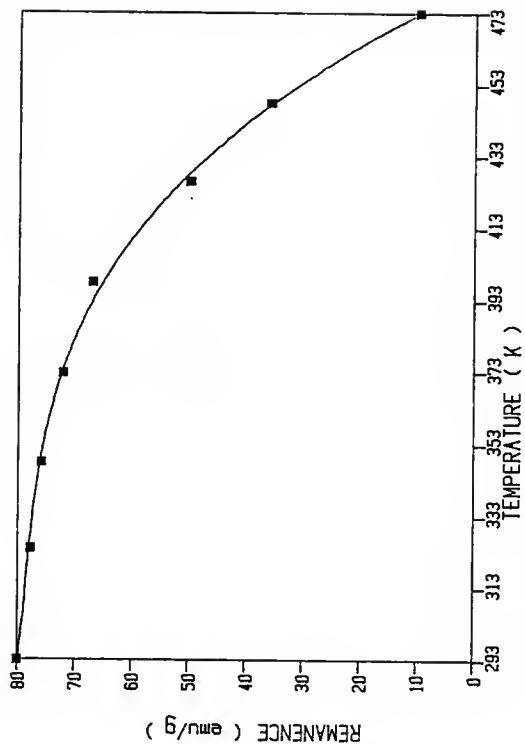


Fig. 6.2.4 Remanence (emu/g) of an $\text{Fe}_{74}\text{Mn}_{13.5}\text{Dy}_{4.8}\text{B}_{7.7}$ sintered magnet as a function of temperature.

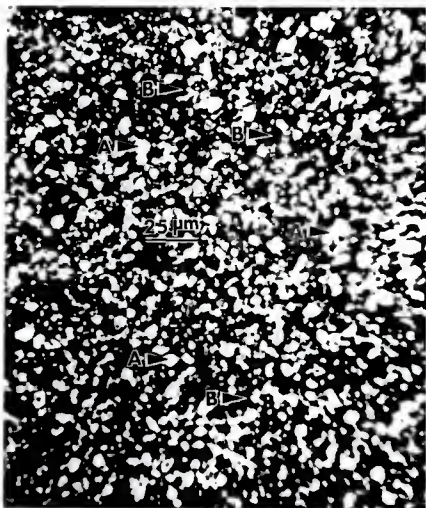


Fig. 6.3.1 Microstructure of $\text{Fe}_{74}\text{Mm}_{13.5}\text{Dy}_{4.8}\text{B}_{7.7}$ sintered magnet obtained using an optical microscope. A= $\text{Fe}_{14}\text{R}_2\text{B}$ phase, B=rare-earth rich phase.

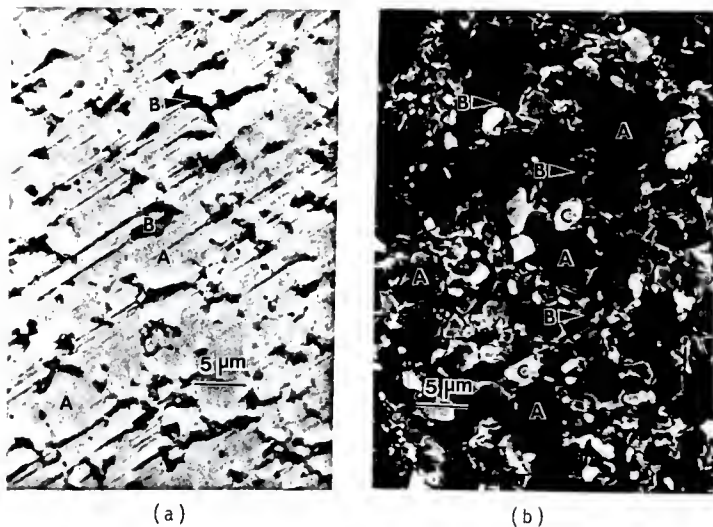


Fig. 6.3.2 Microstructure of an $\text{Fe}_{74}\text{Mm}_{13.5}\text{Dy}_{4.8}\text{B}_{7.7}$ sintered magnet obtained using scanning transmission electron microscope (magnification=2000).

(a) Before etching.

(b) After etching for few seconds using 3% nital.

A= $\text{Fe}_{14}\text{R}_2\text{B}$ phase, B=rare-earth rich phase,

C= $\text{Fe}_4\text{R}_1\text{B}_4$ phase.

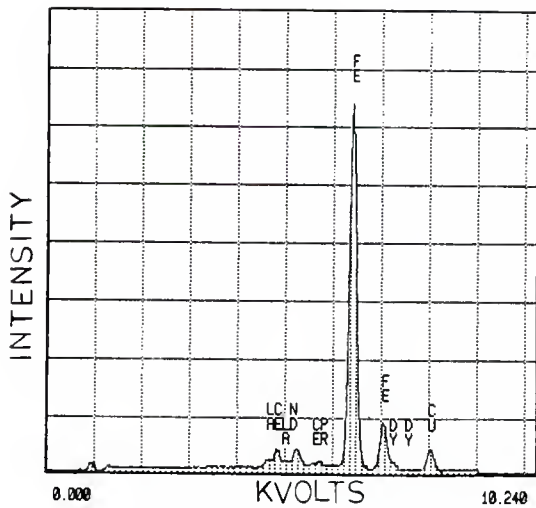


Fig. 6.3.3 Spectra taken using energy dispersive X-ray analyzer in the A regions ($\text{Fe}_{14}\text{R}_2\text{B}$ phase) shown in Figure 6.3.2.

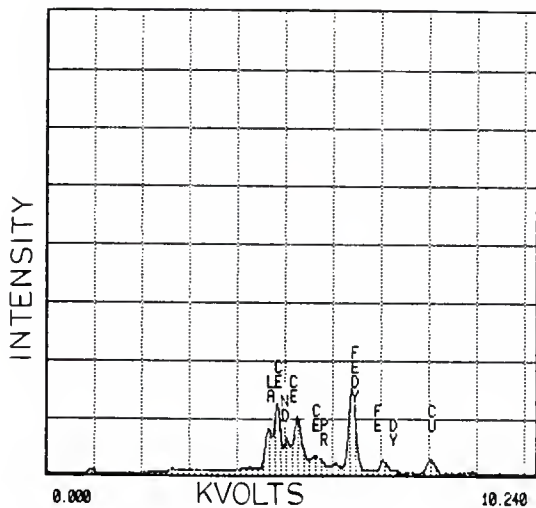


Fig. 6.3.4 Spectra taken using energy dispersive X-ray analyzer in the B regions (rare-earth rich phase) shown in Figure 6.3.2.

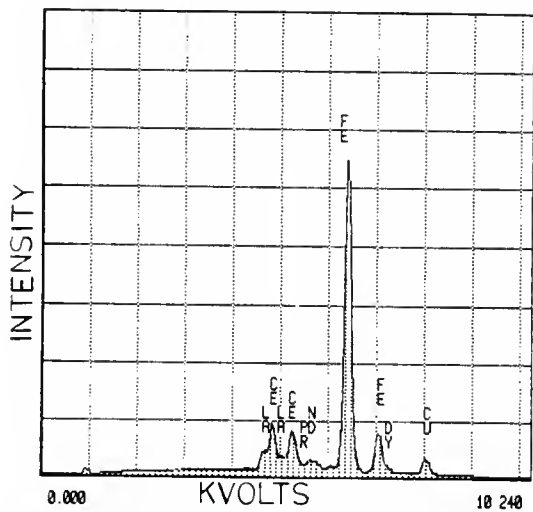


Fig. 6.3.5 Spectra taken using energy dispersive X-ray analyzer in the C regions ($\text{Fe}_4\text{R}_1\text{B}_4$) shown in Figure 6.3.2.

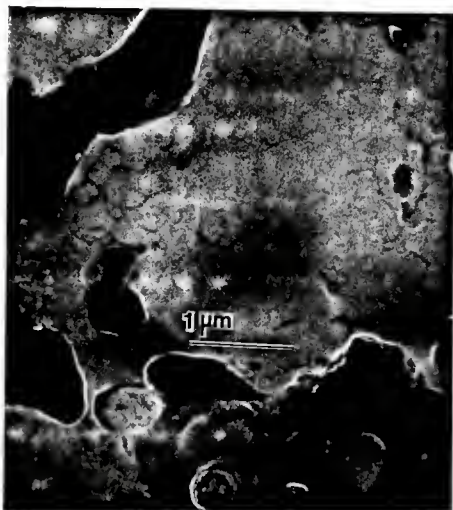


Fig. 6.3.6 Fe₁₄R₂B grains surrounded by inclusions, possibly oxides (magnification=20000).

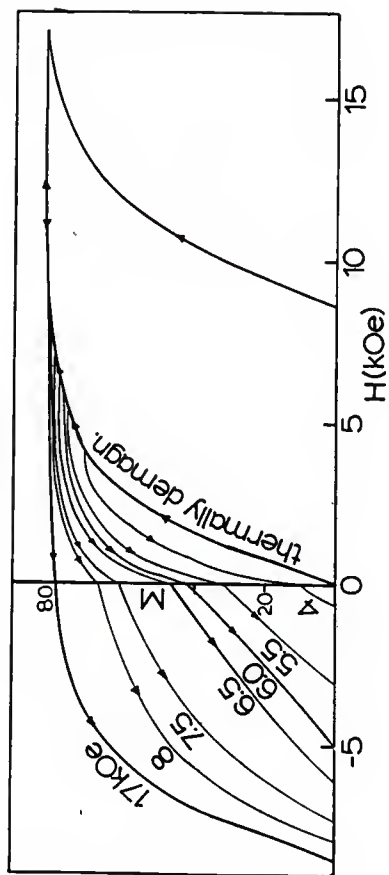


Fig. 6.4.1.1 Magnetization curve and demagnetization curves of a thermally demagnetized $\text{Fe}_{74}\text{Mn}_{13.5}\text{Dy}_{4.8}\text{B}_{7.7}$ magnet.

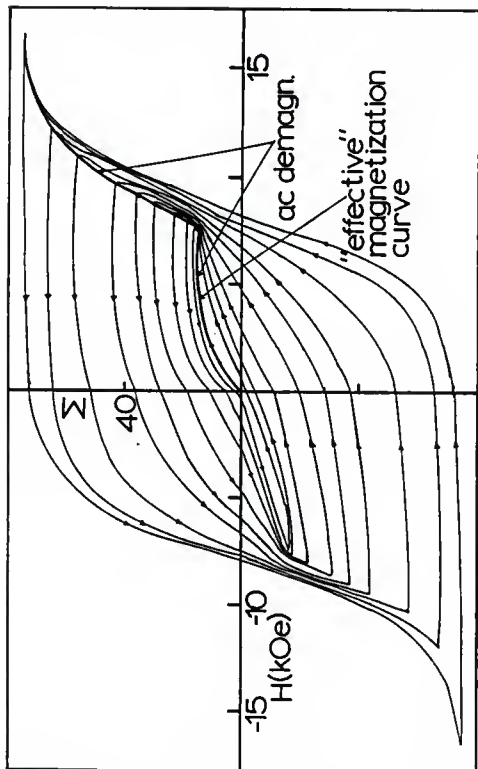


Fig. 6.4.2 Magnetization curve and minor hysteresis loops of an ac demagnetized $\text{Fe}_{74}\text{Mn}_{13.5}\text{Dy}_{4.8}\text{B}_{7.7}$ magnet.

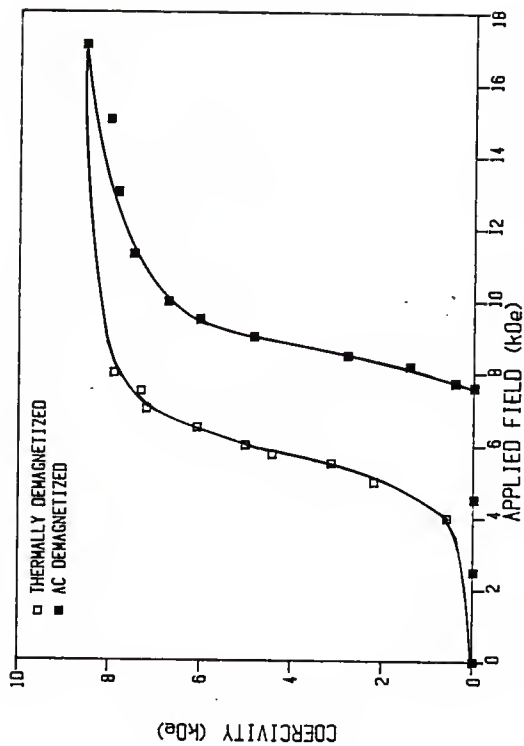


Fig. 6.4.3 Coercivity as a function of the applied magnetic field for a thermally and ac demagnetized $\text{Fe}_{74}\text{Mm}_{13.5}\text{Dy}_{4.8}\text{B}_{7.7}$ magnet. (Refer at Figure 6.4.1 and 6.4.2).

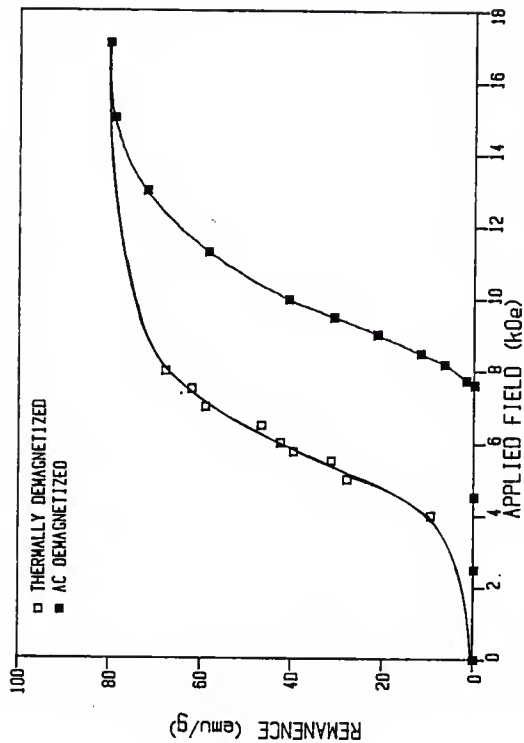


Fig. 6.4.4 Remanence as a function of the applied magnetic field for a thermally and ac demagnetized $\text{Fe}_{74}\text{Mm}_{13.5}\text{Dy}_{4.8}\text{B}_{7.7}$ magnet (Refer at Figure 6.4.1 and 6.4.2).

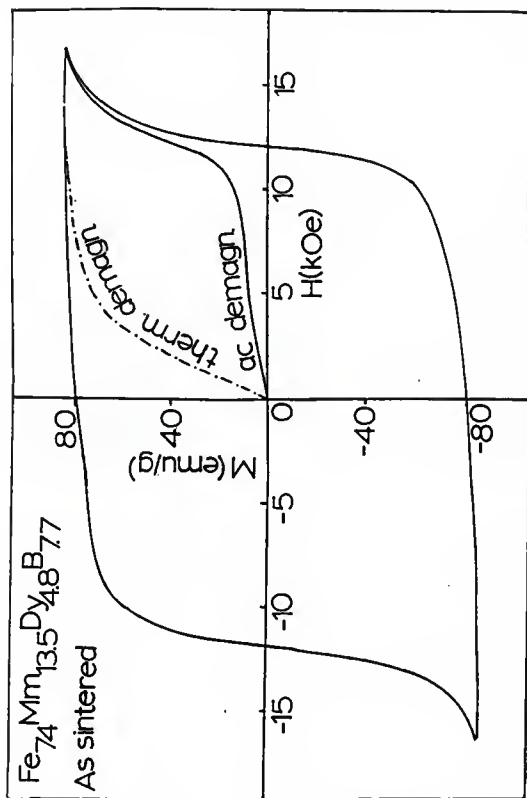


Fig. 6.4.5 Hysteresis loop of the optimum $\text{Fe}_{74}\text{Mm}_{13.5}\text{Dy}_{4.8}\text{B}_{7.7}$ sintered magnet. The magnetization curves in the thermally and ac demagnetized state are shown for comparison.



Fig. 6.4.6 Magnetic domains observed in a thermally demagnetized $\text{Fe}_{74}\text{Mm}_{13.5}\text{Dy}_{4.8}\text{B}_{7.7}$ sintered magnet.

Table 6.2.1

Coercivity (in kOe) and remanence (in emu/g)
of $\text{Fe}_{74}\text{Mm}_{13.5}\text{Dy}_{4.8}\text{B}_{7.7}$ sintered magnet as
a function of temperature (in K).

Temperature (K)	Coercivity (kOe)	Remanence (emu/g)
293	11.30	80.0
324	9.80	77.8
348	8.65	75.6
373	7.30	72.2
398	5.40	66.7
426	2.70	50.0
448	1.80	35.6
473	0.60	10.0

Table 6.3.1

Energy dispersive X-ray elemental analysis (in mole%, based on iron and rare-earths, boron can not be detected) of A ($Fe_{14}R_2B$), B (rare-earth rich) and C ($Fe_4R_1B_4$) regions shown in Fig. 6.3.2.

Regions	A	B	C
Elements (mole %)	Fe ₁₄ R ₂ B	R-rich	Fe ₄ R ₁ B ₄
Fe	87.02	55.65	80.26
Ce	2.91	21.56	8.32
La	1.16	15.01	3.12
(Nd+Pr)	2.19	5.05	3.84
Dy	6.72	2.74	4.46
(Ce+La+Nd+Pr+Dy)	12.98	44.35	19.74

REFERENCES

- [1] K. Strnat, G. Hoffer, W. Ostertag and J.C. Olson,
J. Appl. Phys., **37**, 1252 (1966).
- [2] K.H.J. Buschow, P.A Naastepad and
F.F. Westendorp, J. Appl. Phys., **40**, 4029 (1969).
- [3] T. Ojima, S. Tomizawa, T. Yoneyama and T. Hori
Japan. J. Appl. Phys., **16**, 671 (1977).
- [4] G.C. Hadjipanayis, J. Appl. Phys.,
55, 2091 (1984).
- [5] D. Li and K.J. Strnat, J. Appl. Phys.,
55, 2103 (1984).
- [6] K.S.V.L. Narasimhan, Proceedings of the eighth
international workshop on rare-earth magnets and
their applications, Dayton, Ohio,
6-8 May 1985, p.459.
- [7] H. Nagel, H.P. Klein, and A. Menth,
J. Appl. Phys., **47**, 3312 (1976).
- [8] J.W. Walkiewicz and M.M. Wong,
IEEE Mag., **MAG-15**, 1757 (1979).
- [9] J.J Rhyne, J.H. Schelleng, and N.C. Koon,
Phys. Rev., **B10**, 4672 (1974).
- [10] R.C. Taylor, J. Appl. Phys., **47**, 1164 (1976).

- [11] G.C. Hadjipanayis, S.G. Cornelison, J.M. Gerber and D.J. Sellmyer, *J. Magn. Magn. Mater.*, **21**, 101 (1980).
- [12] A.E. Clark, *Appl. Phys. Lett.*, **23**, 642 (1973).
- [13] N.C. Koon and B.N. Das, *Appl. Phys. Lett.*, **39**, 840 (1981).
- [14] J.J. Croat, *IEEE Trans. Magn.*, **MAG-18**, 1442 (1982).
- [15] G.C. Hadjipanayis, R.C. Hazelton and K.R. Lawless *Appl. Phys. Lett.*, **43**, 797 (1983).
- [16] M. Sagawa, S. Fujimura, N. Togawa, H. Yamamoto, and Y. Matsuura, *J. Appl. Phys.*, **55**, 2083 (1984).
- [17] J.F. Herbst, J.J. Croat, F.E. Pinkerton and W.B. Yelon, *Phys. Rev.*, **B29**, 4176 (1984).
- [18] D. Givord, H.S. Li, and J.M. Moreau, *Solid State Commun.*, **50**, 497 (1984).
- [19] M. Sagawa, S. Fujimura, H. Yamamoto, Y. Matsuura, and K. Hiraga, *IEEE Trans. Magn.*, **MAG-20**, 1584 (1984).
- [20] M. Okada, S. Sugimoto, C. Ishizaka, T. Tanaka, and M. Homma, *J. Appl. Phys.*, **57**, 1 (1985).

- [21] Zhang Maocai, Ma Deking, Jiang Xinling, and Lin Shigiang, Proceedings of the eighth international workshop on rare-earth magnets and their applications, Dayton, Ohio, 6-8 May (1985), p.541.
- [22] J. Yamasaki, H. Soeda, M. Yanagida, K. Mohri, N. Teshima, O. Kohmoto, T. Yoneyama and N. Yamaguchi, IEEE Trans. Magn., **MAG-22**, 763 (1986).
- [23] C.N. Christodoulou, J. Schlup and G.C. Hadjipanayis, "Oxidation of Fe-R-B pouders during preparation of permanent Magnets" to be published (1987).
- [24] C. N. Cristodoulou, J. Schlup and G. C. Hadjipanayis, "Processing of Fe-R-B powders in the preparation of Permanent Magnets" to be published (1987).
- [25] C.W. Chen, "Magnetism and metallurgy of soft magnetic materials", Vol.xv, North-Holland, (1977)
- [26] E.A. Nesbitt and J.H. Wernick, "Rare earth permanent magnets", Academic Press, N.Y (1973).
- [27] "Ferromagnetic Materials", Vol.3, Edided by E.P. Wohlfareh, North-Holland publishing Co. p.44 (1982).

- [28] Allan H. Morrish, "The Physical Principles of Magnetism", John Wiley and sons, Inc., p.335 (1965).
- [29] Y. Matsuura, S. Hirose, H. Yamamoto, S. Fujimara, M. Sagawa and K. Osamura, Japan. J. Appl. Phys., **24**, L 635 (1985)
- [30] R.R. Irani and C.F. Callis, "Particle Size : Measurement , Interpretation and Application", John Wiley , N.Y (1963).
- [31] S. Foner, "Versatile and Sensitive Vibrating-Sample Magnetometer", Rev. Sci. Instr., **30**, 548 (1959).
- [32] ASTM Designation C 135-66, "True density for refractory materials".
- [33] I.V. Mitchell, "Nd-Fe permanent magnets: their present and future applications", Elsevier applied science publishers, N.Y p.85 (1985).
- [34] R.E. Cesh and D.L. Martin, Proceedings of the eighth international workshop on rare-earth magnets and their applications, Dayton Ohio, 6-8 May (1985) p.279.
- [35] L. Eyring, "Progress in the Science and Technology of the Rare-earths", N.Y Pergamon Press, p.336 (1964).

- [36] G.C. Hadjipanayis, J. Appl. Phys. **55**, 2091 (1984).
- [37] J.J. Croat, J.F. Herbst, R.W. Lee and
F.E. Pinkerton, J. Appl. Phys., **55**, 2078 (1984).
- [38] K.J. Strnat, D. Li and H.F. Mildrum,
J. Appl. Phys., **55**, 2100 (1984).
- [39] D. Li and K.J. Strnat,
J. Appl. Phys., **55**, 2103 (1984).
- [40] G.C. Hadjipanayis, K.R. Lawless and R.C. Dickenson
J. Appl. Phys., **57**, 4097 (1985).
- [41] H.H. Stadelmaier, N.A. Elmasry, N.C. Lin
and S.F. Sheng, Materials Letters **2**, 411 (1984).
- [42] Yen-Lung Chen, "Transmission electron microscopy
study of high energy product Fe-Nd-B ribbons",
General Motors Research Laboratories,
February 6, 1985.
- [43] K. Gudimetta, C.N. Christodoulou and
G.C. Hadjipanayis J. Appl. Phys.
Lett., **48**, 670 (1986).
- [44] M.H. Ghandehari, J. Appl. Phys.
Lett., **4**, 548 (1986).
- [45] K.H.J. Buschow, P.A. Naastepad and F.F. Westendorp
J. Appl. Phys., **40**, 4029 (1969).

- [46] D.D. Cullity, "Introduction to magnetic materials"
Addison-Wesley Publishing Company, London (1972).
- [47] D.J. Craik and R.S. Tebble, "Ferromagnetism and
Ferromagnetic Domains", Vol. iv,
John Willey & Sons, N.Y (1965).
- [48] L.F. Bates, "Modern Magnetism",
Cambridge, Bristol (1951).
- [49] D.J. Craik, "Structure and Properties of Magnetic
Materials", J.W. Arrowsmith Limited,
Bristol (1971).
- [50] G.C. Hadjipanayis and C.N. Christodoulou,
"Magnetic Properties of Powdered, Melt-Spun and
Sintered Magnets", to be published (1987).
- [51] G.C. Hadjipanayis, R.C. Dickenson and
K.R. Lawless, J. of Magnetism and Magnetic
Materials, 54-57, 557 (1986).
- [52] Bao-Min MA and K.S.V.L. Narasimhan, J. of
Magnetism and Magnetic Materials,
54-57, 559 (1986).
- [53] J.D. Livingston, Report No 72CRD316,
General Electric, November 1972.

- [54] G.C. Hadjipanayis, R.C. Dickenson and K.R. Lawless, Proceedings of Int. Conf. Magn., Part I, 557 (1985).
- [55] K. Honda and S. Kaya, "On the Magnetization of Single Crystals of Iron", Sci. Reports Tohoku Univ., **15**, 721 (1926).
- [56] S. Kaya, "On the Magnetization of Single Crystals of Nickel", Sci. Reports Tohoku Univ., **17**, 639 (1928).
- [57] S. Kaya, "On the Magnetization of Single Crystals of Cobalt", Sci. Reports Tohoku Univ., **17**, 1157 (1928).
- [58] N.C. Koon, B.N. Das, M. Rubinstein and J. Tyson, J. Appl. Phys., **57**, 4091 (1985).

APPENDIX A

CGS units are used in the present study. The reasons for choosing this system are.

- 1) The instruments provided data in CGS units.
- 2) Most of the literature on hard magnetic materials uses CGS units.

A table of CGS units and the corresponding MKS units is below. The relationships between these units are given also.

<i>cgs</i> units	<i>mks</i> units
$B = H + 4\pi M$	$B = \mu_0 H + M$
B in gauss	B in webers/meter ² (tesla)
H in oersteds	H in amperes/meter
M in emu/cm ³	M in webers/meter ²
μ (vacuum) = 1	μ_0 (vacuum) = $4\pi \times 10^{-7}$ weber/ampere meter
<i>cgs</i> to <i>mks</i>	<i>mks</i> to <i>cgs</i>
B : 1 gauss = 10^{-4} weber meter ²	1 weber/meter ² = 10^3 gauss
H : 1 oersted = 79.6 amperes/meter	1 ampere/meter = 12.57×10^{-3} Oe
M : 1 emu/cm ³ = 12.57×10^{-4} weber/meter ²	1 weber meter ² = 796 emu.cm ³
ϕ : 1 maxwell = 10^{-8} weber	1 weber = 10^8 maxwells

OPTIMIZATION STUDIES AND FABRICATION OF
AN Fe-Mm(Dy)-B PERMANENT MAGNET USING
POWDER METALLURGY TECHNIQUES

by

CHRISTODOULOS N. CHRISTODOULOU

B. S. IN CHEMICAL ENGINEERING
ARISTOTELIAN POLYTECHNION
POLYTECHNIC SCHOOL OF SALONICA-GREECE
1984

AN ABSTRACT OF A MASTERS THESIS

submitted in partial fulfillment of the

requirements for the degree

MASTER OF SCIENCE

Department of Chemical Engineering

KANSAS STATE UNIVERSITY
Manhattan, Kansas

1987

ABSTRACT

An $\text{Fe}_{74}\text{Mn}_{13.5}\text{Dy}_{4.8}\text{B}_{7.7}$ permanent magnet has been developed using powder metallurgy techniques. Optimization studies have been made for all processes steps in order to maximize the hard magnetic properties. The optimum conditions are found to be 1.72 microns for the powder average particle size, 8.0 kOe and 3.3 kbar for the aligning magnetic field strength and compaction pressure, and 1313 K and 1 hr for sintering temperature and time.

The magnetic properties of the optimized magnets are 80 emu/g for the remanent magnetization, 12 kOe for the coercivity and 15 MGOe for the maximum energy product. The degree of alignment ($(M_r/M_s) \times 100$) of the final sintered magnet is 96%. The density achieved at the optimum conditions is 7.31 g/cm^3 .

The effect of oxygen on powders and the resulting sintered magnets has also been investigated. It is found that there is a critical oxygen concentration associated with a critical particle size which limits the development of the hard magnetic properties. This critical oxygen concentration is found to be 0.428 wt% and the associated critical particle size 1.72 microns. The mechanism responsible for the hard magnetic properties is found to be domain wall pinning inside the grains.